Hochschule Bremen — City University of Applied Sciences

School of Nature and Engineering, Department of Mechanical Engineering

HSB

Development of an Optical Far-Field Generator for Intersatellite Laser Interferometers

**Thesis in the Aerospace Engineering degree programme
to obtain the academic degree Bachelor of Engineering**

Submitted by:	Tim Lück
	Matriculation number: 5115268
Submission date:	July 22, 2024
First examiner:	Prof. Dr. Antonio Francisco García Marín
Second examiner:	Prof. Dr. Meike List

Declaration of independent work

I hereby certify that I have written this thesis independently and have not used any sources or aids other than those indicated. The passages in the work that have been taken from other works verbatim or in spirit are indicated by the source.

This declaration also applies to graphics, sketches and illustrations contained in the thesis as well as to sources from the internet. The thesis has not been submitted to any other examination authority with the same content or in substantial parts.

Tim Lück, 5115268

Abstract

This thesis covers the development and characterization of an optical system that provides a laser beam with the key properties of a beam in the far-field. Such a far-field generator is necessary for testing environments of intersatellite interferometers. The resulting beam will be used in such a setup to simulate the received beam from a distant spacecraft and thus be part of the optical ground support equipment. The primary function of the far-field generator is to homogeneously illuminate a receiving aperture with a diameter of 8 mm with a flat wavefront. The thesis investigates different approaches for providing the required beam, describes the design of the optical system and evaluates its performance.

In the developed system, an output beam with homogeneous intensity distribution is achieved by appropriately truncating a wide Gaussian beam. The resulting beam exits the system collimated with a quasi-flat wavefront. Analysis of the beam shows a flat-top intensity distribution and a root-mean-squared wavefront error of $\lambda/46$ at $\lambda = 1064$ nm. The intensity homogeneity in the resulting beam cannot be reliably assessed with the available equipment.

It is concluded that the developed system provides a beam with the main characteristics of a beam segment in the far-field and that further experimental analysis of the intensity distribution is necessary.

Contents

Acronyms

ADC analog-to-digital converter.

DLR German Aerospace Center (Deutsches Zentrum für Luft- und Raumfahrt).

ESA European Space Agency.

FFT Fast Fourier Transform.

GOCE Gravity field and steady-state Ocean Circulation Explorer.

GRACE Gravity Recovery and Climate Experiment.

GRACE-C Gravity Recovery and Climate Experiment Continuity.

GRACE-FO Gravity Recovery and Climate Experiment Follow-On.

LISA Laser Interferometer Space Antenna.

LRI Laser Ranging Instrument.

MAGIC Mass-Change and Geosciences International Constellation.

MFD mode field diameter.

NASA National Aeronautics and Space Administration.

NGGM Next Generation Gravity Mission.

OGSE optical ground support equipment.

PV peak-to-valley.

RMS root-mean-squared.

RoC radius of curvature.

RX-beam received beam.

S/C spacecraft.

1 Introduction

1.1 Space-based geodesy

To understand the large-scale geological and hydrological dynamics of the Earth, it is essential to observe changes in the structure of the planet itself as accurately as possible. The field of geodesy covers those necessary measurements of the size, shape and gravitational field of the Earth. First geodetic observations go back to over 2000 years ago, when the term *geometry* was coined and first estimates of the Earth's radius were made in the third century BC. The continuous drive to gain a more detailed understanding of the Earth's geometry led to the formation of the association *Internationale Erdvermessung* (International Geodetic Association) at the end of the 19th century and for many years geodetic measurements were confined to the surface of the Earth [1].

In recent decades, easier access to space has enabled new methods of high-accuracy Earth observation. While the fields of altimetry and gravimetry are among the main beneficiaries of that development, many other space based measurements are used in the context of geodesy. An overview of the techniques used can be found in an article by S.G. Jin [2]. One remarkable example of satellite geodesy was the Gravity field and steady-state Ocean Circulation Explorer (GOCE). By comparing the acceleration acting on different proof masses inside the spacecraft (S/C), GOCE delivered a very accurate model of the Earth's geoid [3]. In 2002 the Gravity Recovery and Climate Experiment (GRACE) was launched to track changes in the Earth´s gravity field which are mainly induced by the redistribution of water on a large scale. GRACE consisted of two satellites in a near-polar low-Earth orbit, with one following the other at a distance of approximately 220 km. Disturbances in the gravity field were measured by accurately determining the changes in intersatellite distance with a K-Band microwave ranging system [4].

The GRACE Follow-On mission (GRACE-FO) is currently active and heavily inspired by its predecessor in terms of functionality and orbit design. While the main ranging instrument is the same as in GRACE, GRACE-FO also includes a Laser Ranging Instrument (LRI) to demonstrate the capabilities of such a system. The functionality of the LRI is comprehensively described in e.g [5] and [6] among others.
Since its launch in May 2018, 11 months after the decommissioning of GRACE, the follow-on mission has been continuing its observations and showcasing the potential of

intersatellite laser interferometry for geodesy missions. The LRI is the first instance of a laser interferometer being used between two S/C positioned far away from each other and as such it also serves as a technology demonstrator for the prominent Laser Interferometer Space Antenna (LISA) [7][8].

Future GRACE-like missions are being planned by the European and US space agencies ESA and NASA in the frame of the Mass-Change and Geosciences International Constellation (MAGIC) to continue observing mass changes on Earth after GRACE-FO reaches the end of its lifetime. MAGIC will presumably consist of two satellite pairs in a so-called Bender formation [9], with one pair in a polar orbit and the other flying with 63 degree inclination. By using more than one satellite pair, the accuracy of GRACE's gravity field solution can theoretically be surpassed by a factor of up to 200 [10].

The two experiments that are being developed in the context of MAGIC are ESA's Next Generation Gravity Mission (NGGM) and the Gravity Recovery and Climate Experiment Continuity (GRACE-C) led by NASA and the German Aerospace Center (Deutsches Zentrum für Luft- und Raumfahrt; DLR). Building on the success of the LRI demonstrated by GRACE-FO, both pairs will use heterodyne Michelson interferometers as their primary instruments to measure changes in intersatellite distance on a nanometer-scale [11][12]. The increase in accuracy expected from a MAGIC scenario would enable more detailed observations of a number of global mass change phenomena. Some examples are the detection of changes in the amplitude of the global water cycles as a consequence of climate change or analyses of oceanic circulations [13][14].

1.2   Goals and motivation for the thesis

In the context of satellite based geodesy missions, the S/C separations are usually large. For the currently active GRACE-FO experiment as well as the planned NGGM satellite pair, the average separation between the S/C is around 220 km. The laser beam of the interferometer inevitably diverges while propagating over such a large distance and when reaching the distant satellite only a small portion of the beam is sampled by a receiving aperture [5][6][15].

In the case of GRACE-FO, the beam arriving from the other S/C—commonly referred to as the received beam (RX-beam)— has an approximate radius between 20 m and 35 m, depending on the intersatellite distance, which can vary between 170 km and 270 km in the case of GRACE-FO. The wavefront of the laser in the far-field can be viewed as spherical in shape with the center being at the distant S/C. The radius of curvature (RoC) of the wavefront therefore equals the distance of approximately 220 km. The beam is sampled by a receiving aperture with a radius of 4 mm, and although the transversal intensity profile of the beam has a Gaussian shape, the intensity distribution over an 8 mm section can

be considered to be homogeneous with a beam that large. Similarly, the phase variation due to a curved wavefront is negligible over the sampled portion, such that the RX-beam practically has a flat intensity cross-section and wavefront [16].

Note that in this thesis, the term *intensity* refers to the power density in watts per square meter of a laser beam, and unless otherwise specified, the term *radius* refers to the $1/e^2$-radius of a Gaussian beam i.e. the distance from the propagation axis at which the intensity drops to $1/e^2$ of its value on that axis.

To achieve realistic conditions for testing such experiments in a laboratory environment, a beam shaping system is needed which is capable of replicating the key properties of a laser beam in the far-field. The produced beam must be able to evenly illuminate a round receiving aperture of 8 mm in diameter with a flat intensity profile and a flat wavefront. That way, it will mimic an 8 mm section of a laser beam that has propagated as far as in an NGGM or GRACE scenario. This thesis aims to cover the development and characterization of such an optical system. After a conceptual layout has been determined, its capabilities to produce the required RX-beam will be investigated in an experimental setup. The findings from that setup will be the basis for the design of a complete optical assembly intended for use in optical ground support equipment (OGSE) setups of future intersatellite laser interferometers. The initial source will be a laser beam at a wavelength of 1064 nm exiting from a PM980-XP optical fiber with a core diameter of 5.5 μm.

1.3 Beam shaping methods

The need for laser beams with a homogeneous intensity distribution is not limited to the topic of this thesis. There are a number of applications that are improved by using these so-called flat-top beams (or top-hat beams), some examples being photolithography, surface treatment and medical procedures. A detailed overview of the areas where laser beam shaping is commonly used is given by F. Dickey and T. Lizotte in [17] with a more theoretical analysis of the respective methods in the accompanying work [18]. This chapter will only cover a short summary of some techniques used for generating flat-top beams.

Beam homogenizers or uniformizers are optical components that provide an incoming beam with a uniform transversal intensity distribution, disregarding the phase. They are commercially available in different styles. Some use an array of diffracting or refracting elements to form a number of light sources that, when overlapped, create a uniform illumination of the target area. The same effect can be achieved in the form of a homogenizing waveguide called kaleidoscope uniformizer or light pipe, where instead of an array, each internal reflection serves as a light source [17].

There have also been experiments demonstrating the applicability of multimode optical fibers for creating flat-top laser beams. When a beam is channeled from a single-mode waveguide into a short piece of multimode fiber, a large number of higher order modes are excited. Depending on the length and core-diameter of the multimode fiber as well as the wavelength of the laser, a range of intensity profiles can be achieved when the beam exits the fiber. The technique can be used to generate flat-top beams in both the Fresnel and Fraunhofer regions [19].

Field-mappers are optical systems that redistribute the transversal intensity distribution of a laser with a series of diffractive or refractive elements. Commonly a first freeform lens diverts the light depending on the distance from the propagation axis in such a way that the intensity at the second lens is homogeneous. This second lens collimates the beam to form a flat wavefront with a flat-top intensity profile over a certain distance [17][20]. Field-mapping beam-shapers are commercially available and capable of producing flat-top beams with minimal wavefront aberrations and very low power losses. One example is the $\pi Shaper$ [21][22], which is offered for a wide range of wavelengths, including 1064 nm. Laskin and Laskin used the $\pi Shaper$ in conjunction with a Keplerian telescope to illuminate a digital micromirror device with a homogeneous flat-top beam and negligible wave aberrations [23]. While that demonstration used light at 405 nm, the application is still very similar to the topic of this thesis.

Another technique to produce a laser beam with a pseudo-flat intensity profile involves placing a small aperture in the path of a Gaussian beam and only letting the center section propagate farther. Similar to the RX-beam in an intersatellite interferometer, a beam that has been truncated can have a very homogeneous intensity distribution. A far-field generator using that principle was developed for the LISA test-bench and is described in [24]. For many other applications this method is unsuitable because much of the initial power is lost when truncating the beam.

Neither a diffuser nor a setup using a multimode waveguide are practical in the context of this thesis. A diffuser does not produce a spatially coherent beam, so a homogeneous phase profile cannot be achieved. All-fiber beam shapers, including those that use multimode interference, are being used in biomedical applications among others [25] but there is no information available on the achievable quality of flat-top beams and such an investigation would exceed the frame and technical possibilities of this thesis. A commercially available field-mapper like the $\pi Shaper$ seems suitable for the problem. However, the price of such a system exceeds the available budget and the $\pi Shaper$ developers' website states an output beam with a uniformity of 5% [26]. This does not meet the requirements set in section 2.1. Less expensive field-mapping shapers that produce a satisfactory beam are not available for purchase.

The further development will pursue the approach of truncating a Gaussian beam. It is the most promising since the main requirements can be met and it is technically and financially feasible in the context of this thesis. Even though the clipped beam will not have a truly flat intensity profile, the required homogeneity can be achieved when either the incident beam is large enough or the aperture is small enough. Because only lenses and an aperture are used in such a setup, wavefront aberrations are minimal and a flat phase profile can be achieved in the output beam. The inevitable power loss is not problematic for this application, as the same effect also occurs in real intersatellite interferometers. Therefore, a high-power RX-beam is not required for testing purposes and the low efficiency can be considered an advantage. The technique was also used for the flat-top generator described in [24] but the device did not successfully produce a beam with a homogeneous intensity and the phase profile was not measured. Nonetheless, parts of the design can serve as an inspiration and will be built upon in the following chapters.

2 Design and assembly

2.1 Definition of requirements

The following section summarizes the requirements to assure that the system is suitable to be used in future optical bench assemblies. The requirements mainly concern the produced beam.

2.1.1 Beam radius

The size of the produced beam is cruicial for the targeted application. An aperture with a diameter of 8 mm, corresponding to the RX-aperture of the LRI on-board GRACE-FO, must be evenly illuminated. To allow homogeneous illumination even when the far-field generator is misaligned, accidentally or on purpose, the minimal diameter of the flat-top beam shall be 10 mm. The goal is to produce a flat-top beam with a diameter of 15 mm to facilitate alignment and to ensure that potential fluctuations at the beam edge are outside the RX-aperture

2.1.2 Intensity profile

The beam arriving from the far spacecraft in a GRACE- or NGGM-scenario has a radius of approximately 20 m and 35 m, depending on the distance between the satellites. The intensity variation over a 15 mm section of such a beam is negligible and to achieve the same level of homogeneity here is unrealistic. Since laser interferometers use photodiodes to analyze interference of the RX- and local beams, the homogeneity of such a diode can be used as an indicator for the necessary intensity uniformity. A study led by F. Barranco investigated different photodiodes that were considered for future intersatellite laser interferometers and showed that the responsivity of the photodiodes deviates by 1% or more over the active area [27]. It is important to note that this number refers to the spatially resolved response of the investigated photodiodes and that the devices are capable of measuring laser intensity with an accuracy much better than ± 1%.

Nonetheless, a maximum intensity deviation of 1% over the plateau of the produced flat-top beam is set as the design goal. That way the spatial intensity-fluctuations created by the far-field generator are on the same scale as the spatial responsivity of the photoreceivers investigated in [27].

2.1.3 Phase profile

Depending on its radius, the spherical shape of the beams wavefront can cause a phase shift towards the aperture edge. In orbit, the wavefront of the incident beam at the distant spacecraft has a radius of curvature (RoC) corresponding to the intersatellite distance. In a laboratory environment, an RoC of approximately $220\,\mathrm{km}$ can only be achieved through very good collimation, i.e. a beam with negligible divergence. In a similar thesis, the expected wavefront error induced by the optics on the spacecraft gives an indication for the required wavefront radius [24]. There, an RoC of $97\,\mathrm{m}$ is shown to cause the same wavefront error of $\delta = \lambda/33 \approx 32\,\mathrm{nm}$ over an $r_t = 2.5\,\mathrm{mm}$ aperture radius as the S/C optics. The wavefront inhomogeneity δ caused by a spherical wavefront through its sag over an aperture with the radius r_t can be related to the RoC via eq. (2.1). Fig. 2.1 illustrates the geometrical relationship between δ and the radii of the aperture and the wavefront. Solving the Pythagorean theorem for RoC yields:

$$RoC = \frac{r_t^2 + \delta^2}{2\delta} \tag{2.1}$$

An RoC of $248\,\mathrm{m}$ and thus a wavefront sag of $\delta = \lambda/33 \approx 32\,\mathrm{nm}$ over an aperture with a radius $r_t = 4\,\mathrm{mm}$ should also be achieved by the system developed here. With careful lens positioning the RoC can become considerably larger than that value. The majority of the phase errors in the produced beam will not be caused by the spherical shape of the wavefront but rather by the optical components in the setup. Section 2.3.1 and section 2.3.2 cover the selection of the lenses for the far-field generator. The lenses used here are spherical lenses from Thorlabs, which have peak-to-valley (PV) surface irregularities of $h = 147\,\mathrm{nm}$ (stated as $\lambda/4$ at $\lambda = 587.6\,\mathrm{nm}$ in the specifications). According to the manufacturer, the refractive indexes of the N-SF11 and N-BK7 lens materials are $n_{SF11} = 1.78$ and $n_{BK7} = 1.52$. The maximum wavefront error caused by one surface
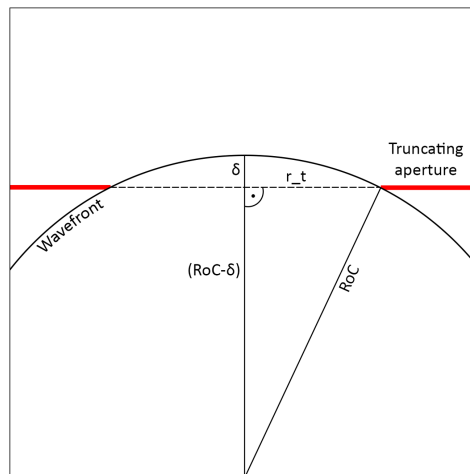
Figure 2.1: *Relationship between the radius of a spherical wavefront and the resulting wavefront sag.*

can be roughly estimated as the change in optical path length $\delta_{surf} \approx h(n-1)$, yielding errors from N-SF11 and N-BK7 lenses of $115\,\text{nm} \approx \lambda/10$ and $76\,\text{nm} \approx \lambda/14$ at $\lambda = 1064\,\text{nm}$, respectively. The resulting effect of the surface irregularities on the wavefront error can only be reduced by using higher quality lenses or minimizing the number of lenses in the system. Spherical lenses can also cause wavefront errors through spherical aberration when the optical path length at the edge of the beam differs from that at the center. Since only spherical lenses are available in the context of this thesis, the resulting wavefront error can only be minimized by choosing the appropriate orientation for each lens (see section 2.4).

The optical system shall include adjustment devices, which allow collimation of the beam corresponding to a wavefront sag of $\delta = \lambda/33$ in the aperture plane. This assures that the irregularities of the lens surfaces are the primary cause of wavefront deviations in the resulting beam and allows future improvement of the system through the usage of higher quality lenses.

2.1.4   Additional requirements

To be practical as OGSE, the system has to be small enough so that it can be incorporated into an optical bench test environment. Therefore, the far-field generator shall not be longer than 50 cm. It should be designed in such a way that the distance from the exit of the system to the RX-aperture is about 20 cm i.e. the requirements described above should be most closely met at $L \approx 20\,\text{cm}$ behind the far-field generator. The final design shall be completely integrated and robust enough to be transportable.

2.2   Conceptual layout

### 2.2.1   A first look at the truncating aperture

The theoretically achievable homogeneity of a truncated beam depends on the ratio of the Gaussian beam width to that of the truncating aperture. This ratio defines the intensity variation in the beam directly after the aperture (see Fig. 2.2). The intensity of a Gaussian laser beam as a function of the distances z and r from its waist and from the propagation axis can be calculated according to A. Siegman [28]:

$$I(r,z) = I_0 \left(\frac{w_0}{w(z)}\right)^2 \exp\left(\frac{-2r^2}{w(z)^2}\right) \tag{2.2}$$

with

$$I_0 = \frac{2P_0}{\pi w_0^2} \tag{2.3}$$

where $w(z)$ is the local beam radius and $w_0 = w(0)$ is the radius at the waist. I_0 is the peak intensity on the propagation axis at the waist and P_0 is the total power of the beam.
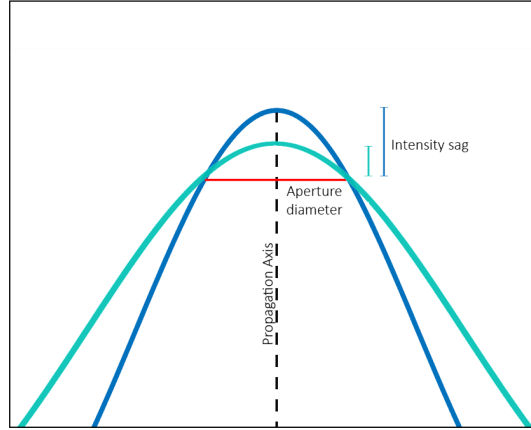
Figure 2.2: *Two Gaussian intensity profiles centered on an aperture.*

Assuming the beam is centered in a circular truncating aperture with the radius r_t, a 1% intensity variation corresponds to the requirement that the intensity at the aperture edge shall vary from the intensity in the center of the beam by less than 1%:

$$\frac{I(0,z)}{I(r_t,z)} \leq 1.01 \tag{2.4}$$

Combining with eq. (2.2) and simplifying then leads to the design requirement:

$$r_t \leq w(z)\sqrt{\frac{\ln{(1.01)}}{2}} \tag{2.5}$$

Equation (2.5) can be used to determine the size of the truncating aperture and shows that the required radius is only dependent on the beam size in the aperture plane.

2.2.2 Comparing layout options

In practice, two main approaches can be used to create the desired ratio of Gaussian beam width to truncating aperture diameter. As discussed above, this ratio is decisive in creating the desired beam. The beam can either be expanded to a large size, allowing a truncating aperture that is 15 mm in diameter, or the incident beam can be clipped at a smaller diameter requiring expansion of the flat-top beam afterwards.

The second approach is used for the LISA telescope simulator described by C. Baune in [24]. There, a Gaussian beam is split off from the main optical bench, expanded in a Galilean telescope and truncated by a pinhole with a radius of 0.15 mm. A single lens is used to image the aperture plane on the target plane, simultaneously expanding it to a radius of 2.5 mm. The approach is illustrated in Fig. 2.3. The experimental section of the work shows that the imaging lens could not be positioned with the necessary accuracy, leading to visible diffraction effects from the pinhole in the target plane. It is also shown that a larger truncating aperture leads to a larger diffraction-less region behind the aperture,
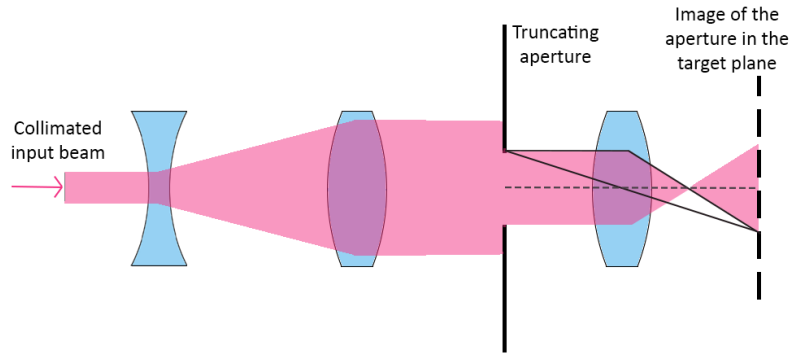
Figure 2.3: *Conceptutal sketch of the approach used by C. Baune [24].*

facilitating the imaging of the aperture stop without noticeable diffraction effects. Such a setup can be used in this thesis if the minimal size of the truncating aperture is considered in the design process. Instead of splitting a beam on the optical bench, a fiber-collimator would be used to decouple the laser from an optical fiber. The separate light source is necessary for the beam shaper to work independently from the main optical bench. A collimator that is already available in the laboratory is the ThorLabs TC25APC-1064, which produces a Gaussian beam with a radius of approximately 2.2 mm. According to eq. (2.5) the required clipping aperture for that beam has a radius of 0.17 mm. That value is close to the size that Baune shows to be too small to work with, so a beam-expanding telescope would be needed. Instead of expanding the beam after a fiber collimator, a layout is possible where the beam propagates directly from the optical fiber until it reaches the desired radius. To magnify the flat-top beam behind the truncating aperture, a telescope would be used in place of a single imaging lens. The reason is the required phase profile. If an aperture plane is imaged with only one lens, the beam will be focused between the lens and the image plane. This leads to a strongly curved phasefront in the target plane. In contrast, a telescope can produce a collimated beam with a quasi-flat wavefront.

A similar approach is described by Sizova et al. in [29] and [30] and illustrated in Fig. 2.4. The incident collimated beam is truncated by an aperture and afterwards passes through a spatial filter. In this case the aperture has a serrated edge to minimize diffraction effects during further propagation. The serration results in a smoother transition from total transmissivity to total blockage at the edge compared to a regular circular aperture. The topic of apodizing and serrated apertures is revisited in section 2.3.3 of this thesis. Since such serration leads to an angular dependence of the electric field after the aperture, the proposed beam shaper uses a spatial filter to remove those variations. The spatial filter consists of a Keplarian telescope with a pinhole at the focus point. The flat-top beam can be expanded to the desired size in the same step. A further improvement is
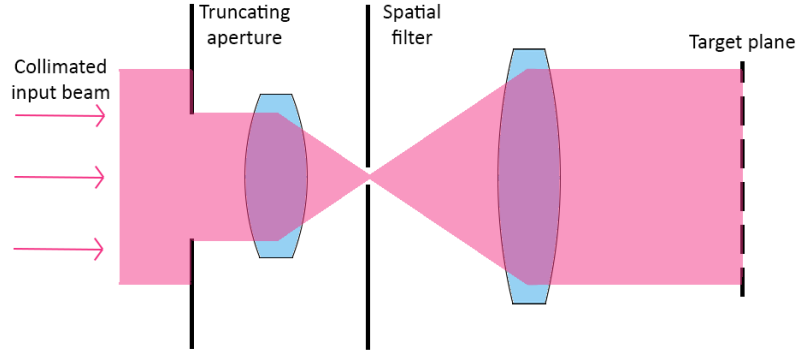
Figure 2.4: *Conceptual sketch of the approach described in [29]–[31].*

proposed in [31] in the form of an opaque corrective ring in the outer region of the serrated aperture. According to the authors, a beam produced in this way can keep its flat-top characteristics over distances up to Fresnel numbers 2-5 (multiple meters for a 1064 nm laser, when the truncating aperture has a radius of e.g. 5 mm). It should be noted that the considerations in [29]–[31] are purely theoretical. Although the concept was patented in the Russian Federation from 2015 to 2019 [32], no experimental verification of the calculated performance is available. Since the output beam of such a setup is collimated, it can be considered a far-field generator. However, all calculations presented by Sizova [29][30][31] are based on the assumption that the incident beam is collimated and as mentioned above, using the TC25APC-1064 fiber-collimator would require a very small aperture diameter. Since manufacturing a serrated aperture of that size is not feasible in the context of this thesis, a beam expander would again be necessary. Considering that every lens can lead to aberrations in the output beam, a solution that requires fewer lenses is preferred. Additionally, a corrective ring according to [31] cannot be manufactured in the context of this thesis, further limiting the potential of such an approach.

The concept pursued in this work is a streamlined version of the ones described above. The beam exiting the fiber is not collimated and instead passes a concave lens to increase the divergence angle. In theory the fiber acts as a mode-cleaner, and the beam exiting the bare fiber end is in the fundamental Gaussian mode with a diameter in the order of the core-diameter. Section 3.1 shows this assumption to be flawed for the used fiber. The beam propagates after passing the first lens until the radius is large enough so that a truncating aperture with a diameter of 15 mm satisfies eq. (2.5). The beam is then clipped to the desired size. Now having a manageable diameter again, the beam is collimated by a single lens to give it a flat phase profile. This layout does not require beam-expansion before and after the truncating aperture and no fiber-collimator, reducing the number of lenses significantly. Some challenges that need to be considered in the design are securely
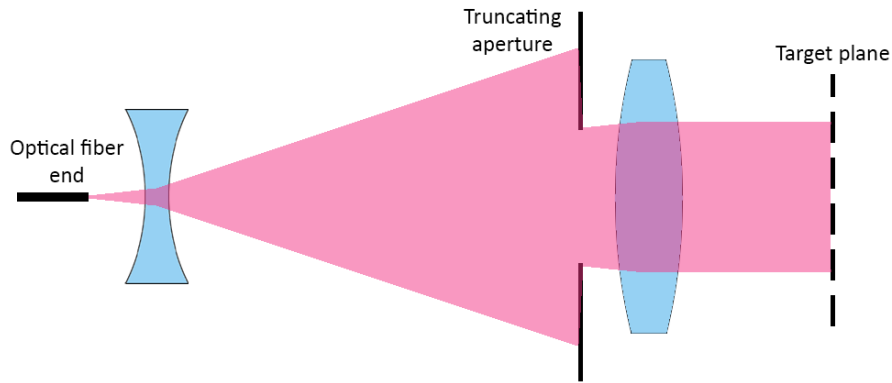
Figure 2.5: *Conceptual sketch of the approach pursued in this thesis.*

attaching the bare fiber end and shielding the large amount of stray light that is produced during the magnification. A high angle of incidence on the second lens caused by the strong divergence can also be problematic. Hence the aperture is placed in front of the lens and the central section that actually reaches the collimating lens does so under a normal angle of incidence.

2.3   Design of the far-field generator

The following section describes the design of the far-field generator following the concept summarized in section 2.2.2. First, the necessary beam expansion before the aperture is considered. Afterwards, a lens is chosen to collimate the produced beam. The truncating aperture is treated in section 2.3.3 before a description of the complete assembly follows. Fig. 2.11 and Fig. 2.12 give an overview of the completed design. Parts of the design are based on simulations conducted with the software tools JamMt and MATLAB. JamMt is a mode matching tool that allows the simulation of Gaussian beam propagation. The simulations included in this thesis use JamMt version 0.24. Simulations in MATLAB use the OSCAR add-on. OSCAR calculates the propagation of light through the Fast Fourier Transform (FFT) of electromagnetic fields [33]. More about the OSCAR add-on and the custom MATLAB functions that were used can be found in Appendix B.

2.3.1   Beam expansion

To create a beam that is 15 mm in diameter, the truncating aperture must have a clear radius of $r_t = 7.5$ mm. According to eq. (2.5) the necessary beam radius just before the aperture for a maximum intensity variation of 1% is $w(z) \approx 106$ mm. For a Thorlabs PM980-XP optical fiber the manufacturer specifies a $1/e^2$ mode field diameter (MFD) of

6.6 µm at a wavelength of 980 nm in the near field. Since the MFD of a waveguide is wavelength-dependent, Marcuse's equation is used to adjust the specified value [34][35].

$$MFD = 2r_c \left(0.65 + \frac{1.619}{V^{3/2}} + \frac{2.879}{V^6} \right) \tag{2.6}$$

with

$$V = \frac{2\pi}{\lambda} r_c NA \tag{2.7}$$

where r_c is the radius of the fiber-core, λ is the wavelength and NA is the numerical aperture of the fiber. Plugging the values $r_c = 2.75\,\mu m$ and $NA = 0.12$ from the manufacturer's specifications as well as $\lambda = 1064\,nm$ into eq. (2.6) gives a mode field diameter of approximately $MFD = 7.14\,\mu m$. For a wavelength of $\lambda = 980\,nm$ the equation yields $MFD = 6.64\,\mu m$, agreeing with the specifications.

It is assumed that the beam exiting the waveguide can be approximated as a Gaussian beam with a waist diameter equal to the MFD of the fiber and the waist position being the fiber end. The rate at which such a beam increases in size can be specified by the divergence angle θ which is the angle between the linearly increasing beam radius and the propagation axis. The assumption that a Gaussian beam grows in a linear fashion only holds true when the distance from the waist is much larger than the Rayleigh range z_R of the beam [28].

$$\theta = \frac{\lambda}{\pi w_0} \,, \qquad for\ z \gg z_R \tag{2.8}$$

where

$$z_R = \frac{\pi w_0^2}{\lambda} \tag{2.9}$$

In the above equations, λ is again the wavelength and w_0 is the waist radius of the beam. For the considered beam eq. (2.9) gives $z_R = 38\,\mu m$, making linear divergence a valid approximation after a few millimeters. Based on eq. (2.8) the beam is expected to propagate with a divergence angle of $\theta = 5.4°$ after the fiber end. The trigonometric relation between the divergence angle and the beam size in the far-field ($z \gg z_R$) is:

$$\theta = \arctan \left(\frac{w(z)}{z} \right) \tag{2.10}$$

To reach the necessary radius in the clipping plane, the beam would have to propagate for over 1 m, making the system impractically long.
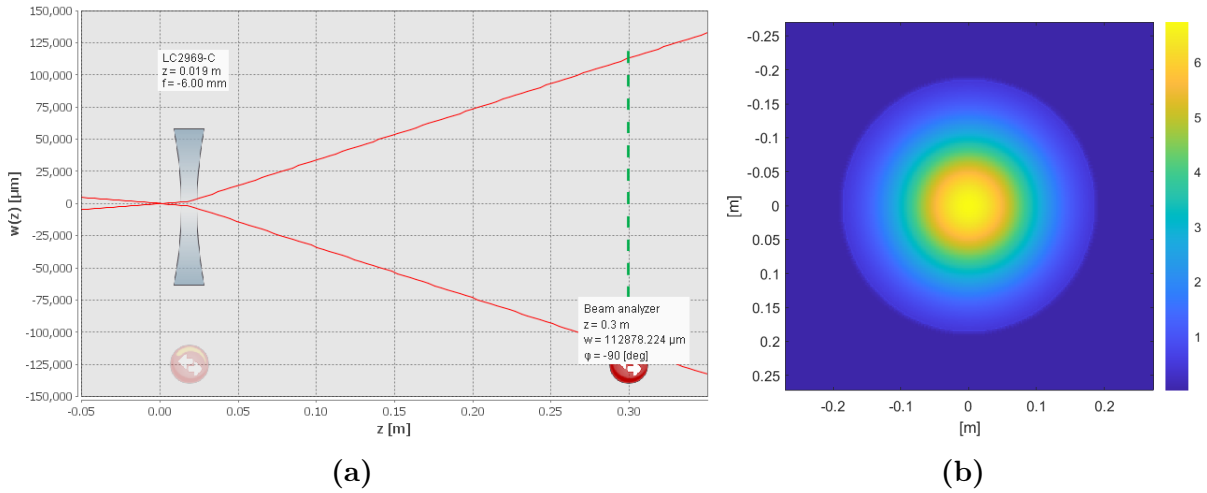
Figure 2.6: *Simulation of the beam passing through an $f = -6$ mm lens positioned at $z = 19$ mm. The waist is $w_0 = 3.57$ μm at $z = 0$ m. (a) JamMt calculation of the beam width. (b) MATLAB/OSCAR calculation showing the amplitude [V/m] of the electric field of the beam at $z = 30$ cm. The clear aperture of the lens is set to 6 mm and the initial field has a power of 1.2 mW.*

A plano-concave lens with a focal length of $f = -6$ mm considerably amplifies the beam divergence. A Thorlabs LC2969-C lens is chosen because it has the shortest focal length while still being easily available. Simulation with JamMt shows that placing the lens 19 mm behind the fiber end leads to a beam radius of $w \approx 113$ mm at $z = 30$ cm from the fiber end (see Fig. 2.6a). The simulation also shows that the resulting beam is not very sensitive with respect to the lens position. A positioning error of up to 1.5 mm still produces an acceptable beam radius of 107 mm at $z = 30$ cm. Since the LC2969-C lens has a diameter of only 6 mm and JamMt calculates a beam diameter of approximately 4.4 mm at the lens position, the setup was also simulated using MATLAB/OSCAR (see Fig. 2.6b). To display the electromagnetic field in the conventional unit volts per meter, resulting fields calculated using OSCAR are adjusted with a factor of $\sqrt{2\eta}$ where η is the free space wave impedance. The results show no significant diffraction effects or noteworthy power loss from the clip at the $f = -6$ mm lens.

A larger lens cannot be used because a larger lens diameter is only commercially available in conjunction with a longer focal length. Therefore, the expanding lens would have to be positioned farther away from the fiber, where the beam diameter is also larger, to achieve the needed divergence. Simulation in JamMt shows that this change in position compensates the benefit of a larger lens diameter. The shortest focal length $f = -6$ mm is chosen because it results in the shortest distance between the optical fiber and the first lens, enabling the joint mounting of the two. This is advantageous because it facilitates the exact adjustment of the distance between the divergent and the collimating lens as section 2.4 shows.
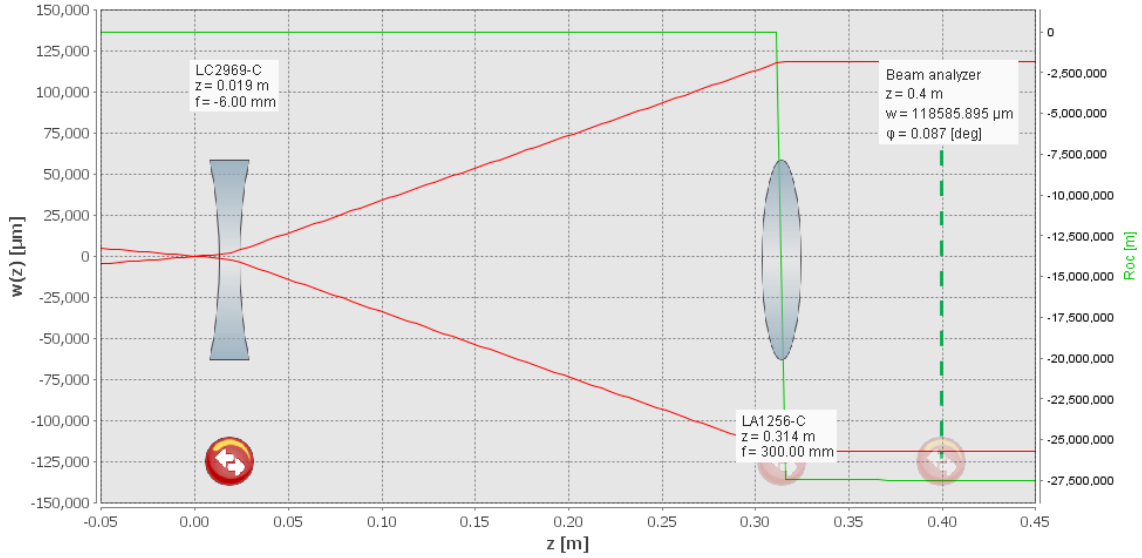
Figure 2.7: *JamMt calculation of the beam width (red) and the RoC (green). An $f = 300$ mm lens is positioned at $z = 314.44$ mm (rounded to millimeters in the figure). The initial beam and the left lens are the same as in Fig. 2.6a*

2.3.2 Collimating lens

To collimate the output beam, a second lens with a positive focal length must be placed at the end of the optical system. If that second lens is positioned with high accuracy, the wavefront RoC approaches infinity in the target plane and with no other aberrations present, the phase profile will become perfectly flat (see eq. (2.1)). The collimating lens is placed behind the truncating aperture to avoid illuminating the complete lens since at that point, the beam radius is much larger than any available lens and the effects that would occur at the lens edges or mount are unpredictable. A lens with a focal length of $f = 300$ mm at $z = 314.44$ mm behind the fiber end produces a beam that is very well collimated at an RoC of $27\,500$ km (see Fig. 2.7). The quality of the collimation is fairly sensitive to displacement of the lens. Adjusting the lens position in the simulation by $10\,\mu$m in either direction results in an RoC of 9 km and an adjustment by $20\,\mu$m results in an RoC of 4.5 km (these are the resulting wavefront radii, not the deviations from the value above). While those values are still acceptable according to section 2.1.3, the best possible collimation is targeted at distance of $L = 20$ cm behind the collimating lens. A positioning accuracy on the micrometer-scale is feasible here.

The ideal lens position being farther from the fiber end than the 30 cm examined in section 2.3.1 is necessary because not the collimating lens, but the truncating aperture needs to be placed at a location where eq. (2.5) is satisfied. An LA1256-C lens by Thorlabs is chosen. With the principal plane positioned at $z = 314.44$ mm, the plano side sits at $z = 311.04$ mm. The truncating aperture must be positioned such that the beam clipping occurs at most 11 mm before the plano side of the second lens.

2.3.3   Revisiting the truncating aperture

Plugging the findings from the simulation in the previous section (see Fig. 2.6a) into eq. (2.5) shows that the intensity drop over an aperture with a 15 mm diameter at $z = 30$ cm is less than 1% in the given beam. This section covers considerations concerning the aperture shape to ensure a stable beam behind the aperture. It is assumed that the collimating lens directly behind the aperture has no effect on the diffraction which results from the truncation.

The target plane where the beam properties have to match the requirements is at a distance of $L = 20$ cm behind the end of the far-field generator but the diffraction at a circular, hard aperture leads to a degradation of the flat-top profile, which can already be problematic over short distances. A way to characterize the diffraction behind such an aperture is the Fresnel number N, which is only dependent on the aperture radius r_t, the distance from the aperture L and the wavelength λ [28].

$$N = \frac{r_t^2}{L\lambda} \tag{2.11}$$

In the near-field, where $N \geq 1$, Fresnel diffraction occurs. For an aperture radius $r_t = 7.5$ mm this region spans several meters. The resulting intensity distribution in the Fresnel region is radially symmetric with diffraction rings extending inwards from the aperture edge. A cross-section of the pattern shows these rings as ripples on the edges of the intensity profile (see Fig. 2.9). Furthermore, high frequency intensity variations occur around the propagation axis. These variations have the form of a Bessel function, which is subtracted from the field for even N or added to it for odd N. For a uniformly illuminated aperture, the magnitude of the Bessel function causes the on-axis intensity to drop to zero or spike to four times the base intensity at integer Fresnel numbers [28]. This is the inverse of the effect which occurs when a circular obstacle is placed inside a laser beam where it is called the spot of Arago or the Poisson spot. If the aperture is not uniformly lit but truncates a Gaussian beam, those central ripples are smoothed depending on the relative intensity at the aperture edge. Here, the relative intensity at the aperture edge is larger than 0.99 by design, hence the smoothing effect is minimal.

While the diffraction rings in the outer region of the beam become more prominent at longer propagation distances, the central intensity variations occur with the same magnitude throughout the Fresnel region. Only the frequency of the underlying Bessel function changes and thus the affected central region is smaller at shorter distances. The Bessel function has the form $J_0(2\pi N r/r_t)$, where r is the distance from the propagation axis and the other variables are as defined above [28]. At 20 cm behind an aperture with $r_t = 7.5$ mm, the Fresnel number is still very large at $N \approx 264.3$ (see eq. (2.11)). In this region the central intensity fluctuations occur at a very high spatial frequency. Fig. 2.8 shows a plot
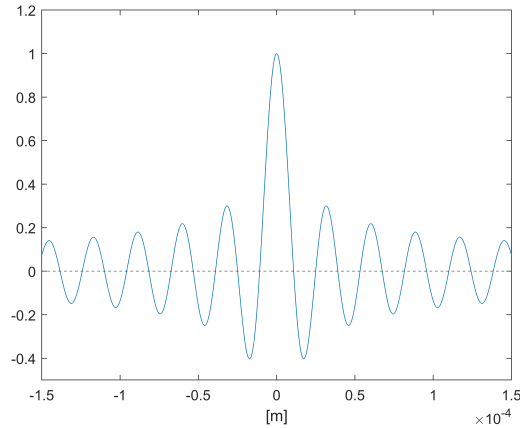
Figure 2.8: *Normalized $J_0(2\pi N r/r_t)$ Bessel function describing the high-frequency central intensity fluctuations at $N \approx 264.3$ behind an $r_t = 7.5$ mm round aperture.*

of the underlying Bessel function, where it is apparent that the peaks are very narrow with the central maximum being approximately $20\,\mu m$ wide. That scale corresponds to only a few pixels in the simulations and measurements that follow. In the experimental setup the phenomenon is partially suppressed by the aperture being not perfectly round and having a slightly transient transmissivity at the edges (see section 3.3). While the magnitude of the central intensity peak is reduced by an imperfect aperture, the effect does still occur. The fact that the affected region of the beam is too small to be investigated with the available equipment (the beam analyzer used in chapter 3 has an effective pixel size of $12.5\,\mu m$) means that the resulting beam would have an unknown intensity peak at its center.

The phenomena described above can also be seen in simulations carried out with MATLAB/OSCAR. The results in Fig. 2.9 show the quasi-flat central section of a Gaussian beam inside a round aperture. After $L = 20$ cm prominent diffraction rings caused by the aperture edges can be seen. At longer propagation distances, the region affected by the central intensity fluctuations is large enough to be visible in the simulation results. This is exemplified for $L = 80$ cm in Fig. 2.9c. The magnitude and spread of the diffraction patterns vary when the resolution of the simulation is changed. Therefore, no exact predictions can be made about the severity of these phenomena in a real application. It is clear, however, that truncation with a hard, circular aperture does not provide a stable flat-top beam, and instead, an aperture design is needed which suppresses diffraction at the beam edge.

An aperture with a gradual transition from total transmissivity to total blockage, rather than a sharp edge, can significantly reduce the mentioned diffraction effects on the beam properties. Since an aperture with a gradual radial change in transmissivity cannot be manufactured in the context of this thesis, a binary aperture must be used to approximate such an apodizing aperture. In [36] and [37] W. Cash presents an apodization function that

(a) *In the aperture plane*   **(b)** *After* 20 cm   **(c)** *After* 80 cm
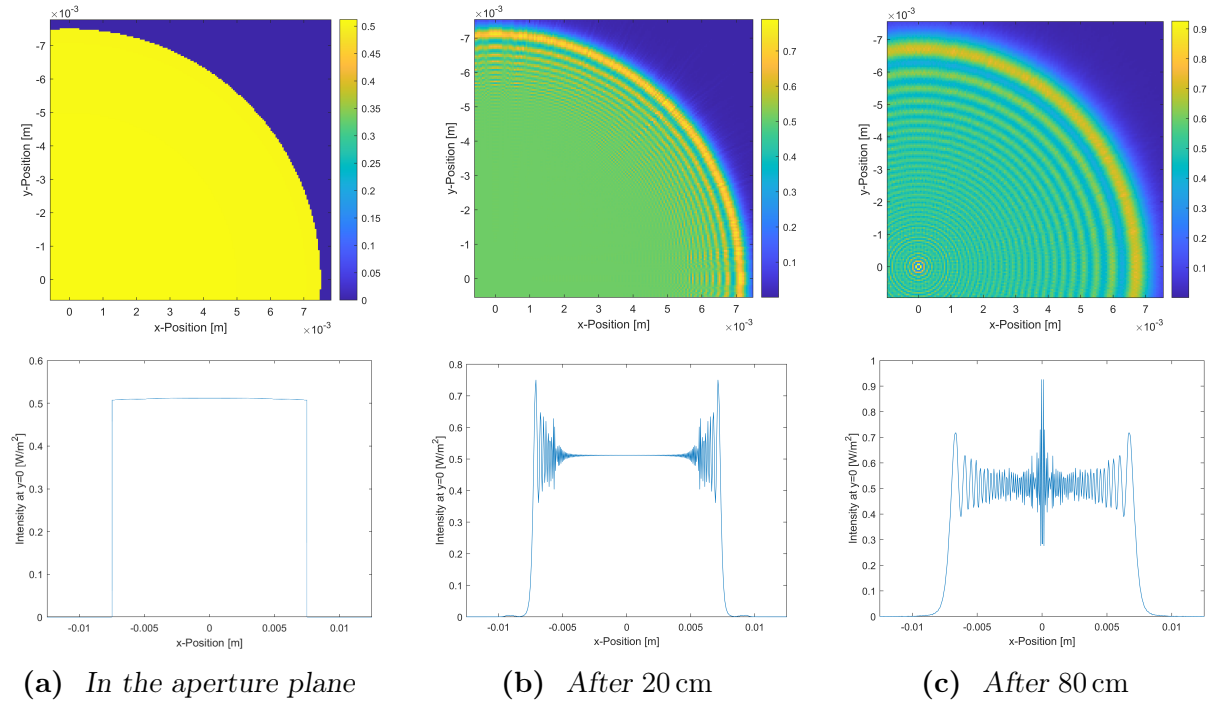
Figure 2.9: *MATLAB/OSCAR simulation of the propagation after a $r_t = 7.5$ mm round aperture. The incident beam is collimated with a radius of $w \approx 113$ mm. The first row shows a section of the intensity distribution in W/m^2 and the second row the corresponding cross-section profile. The pixel size is ≈ 50 μm.*

greatly reduces diffraction effects behind an occulting shield or a starshade. According to Cash the ideal transmissivity progression of a uniformly illuminated obstacle as a function of the distance r from its center is a so-called offset hyper-Gaussian of the form:

$$A(r) = 0 \qquad for\ r < a \tag{2.12}$$

and

$$A(r) = 1 - exp\left(-\left(\frac{r - a}{b}\right)^n\right) \qquad for\ r > a \tag{2.13}$$

where a is the radius within which the transmissivity is zero and b and n define the steepness of the transmissivity curve. Cash also presents a binary starshade design that results in offset hyper-Gaussian apodization by having a central region where all light is blocked and petal-shaped sections at the edges which, when averaged, create a smooth transition to total transmissivity. Dividing the aperture edge into 12 or more petal sections approximates circularly symmetric apodization [37].

In [38][39][40] this concept is used to produce a quasi-flat-top beam for a LISA optical test bench by placing a binary apodizing aperture in front of a commercial fiber collimator. The aperture shape is strongly influenced by Cash's concept and optimized through Monte Carlo simulation. The aperture has a clear central section and 14 petal-shaped
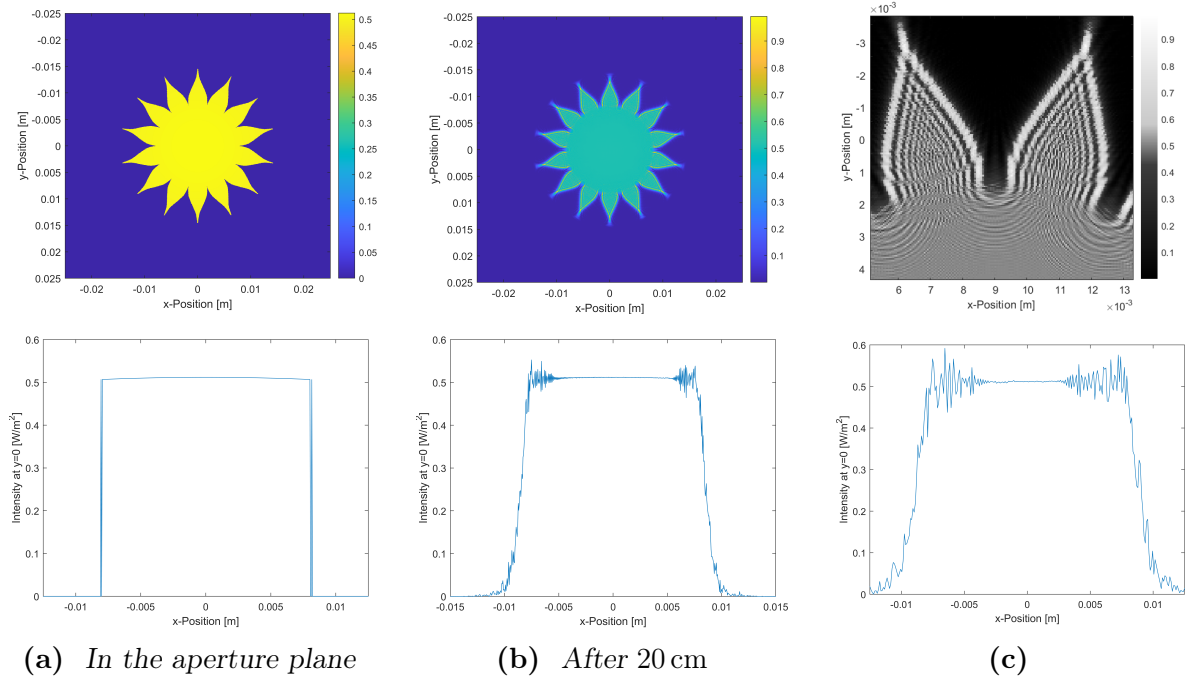
Figure 2.10: *MATLAB/OSCAR simulation of the propagation after an apodizing aperture with a clear diameter of* 16.2 mm. *The incident beam is collimated with a radius of* $w \approx 113$ mm. *For (a) and (b) the first row shows a section of the intensity distribution in* W/m^2 *and the second row the corresponding cross-section profile. (c) Shows a cross-section of the intensity after* 80 cm *on the bottom and a detailed view after* 20 cm *in the top row in a monochrome color-scale for enhanced contrast. The pixel size is* ≈ 50 µm.

cutouts around its circumference. Part of the beam propagates through the clear section undisturbed and the unique edge-geometry prevents unwanted diffraction effects between the collimator and the RX-aperture.

For the truncating aperture of the far-field generator developed here, the edge geometry is adopted from [40]. The clear central region has a diameter of approximately 16.2 mm to prevent visible diffraction effects from the petal-tips to enter the central 15 mm of the beam. While the ripples from the petal-tips do infringe on the flat area of the beam with longer propagation, the otherwise problematic intensity variations at the center are avoided completely (see Fig. 2.10c). The simulation results in Fig. 2.10 show that large parts of the beam remain unaffected by the diffraction at the hard aperture edges over at least 20 cm, proving an apodizing aperture to be an appropriate tool for truncating the expanded beam.

Figure 2.11: *CAD-model of the optical system. The beam path is depicted in red.*

2.4   Assembly of the components

A caging system is chosen to assemble the individual components into a standalone optical system. In a caged assembly the transversal position of the components is fixed by four rods and the position along the optical axis can be adjusted by sliding the components along those rods. Fig. 2.11 shows a CAD-model of the complete cage assembly.

The PM980-XP optical fiber is attached to a terminated fiber adapter with an FC/APC connector. Since the angular position of the polarization-maintaining stress rods inside the waveguide is fixed with respect to the orientation of the FC/APC connector, the angular position of the latter can be used to determine the polarization of the light exiting the fiber. The polarization state of the light has no effect on the functionality of the far-field generator and must be adjusted according to the use-case. A variable fiber attenuator (VOA1064PM-APC from Thorlabs) is installed before the optical fiber that provides the laser for the far-field generator. This is to enable adjustment of the beam's power during use. For all following measurements the least possible attenuation is employed ($\approx 1.3\,\text{dB}$), resulting in a total laser power of approximately $1.2\,\text{mW}$.

Behind the fiber adapter, the $f = 6\,\text{mm}$ lens is held by a 3D-printed adapter such that its back principal plane lies $19\,\text{mm}$ from the emission surface of the fiber (see Appendix A for more detailed information on the fiber adapter). This adapter is designed in such a way that it centers a lens with a diameter of $6\,\text{mm}$ in an internally SM1-threaded lens mount while also acting as a spacer between the fiber adapter and the lens. In contrast to commercially available lens adapters, the clear aperture of the lens is not reduced because the adapter does not use a retaining lip. The adapter is manufactured using a Formlabs Form 3+ resin printer with a dimensional accuracy of $\geq 40\,\mu\text{m}$ [41], which defines the axial position with sufficient accuracy according to section 2.3.1. Both the terminated fiber adapter and the lens spacer are mounted inside the same lens tube, which is in turn mounted to a z-axis translation mount. This allows for simultaneous adjustment of their axial position over approximately $2\,\text{mm}$ with micrometer accuracy. Very accurate adjustment of the distance between the components in the lens tube and

the collimating lens is necessary in order to create the required collimated output beam. To minimize spherical aberration, both lenses are oriented with the plano side facing the highly divergent beam between them.

At $z \approx 30\,\mathrm{cm}$ behind the terminated fiber adapter the truncating aperture and the collimating lens are mounted in the same SM2-threaded cage plate. The aperture is separated from the plano side of the $f = 300\,\mathrm{mm}$ lens only by a retaining ring. The aperture is manufactured using the same 3D-printer as for the lens adapter with a 45 deg chamfer ensuring a clearly defined aperture edge. Cage covers placed along the larger 60 mm section of the cage are used to block off strongly divergent parts of the beam and shield the laboratory from straylight (not pictured in the CAD-rendering). The assembly uses two different cage sizes because the z-translational mount is only available for the 30 mm cage system and the apodizing aperture would not fit into a cage plate of that size. The 30 to 60 mm cage adapter is positioned as closely behind the lens tube as possible so that the beam passes through the 1 inch bore while it is still small. Optical posts are attached to M4 bores on both cage plates and the assembly is mounted on a $15 \times 45\,\mathrm{cm}$ breadboard such that the beam path is elevated 10 cm from the mounting surface. Fig. 2.12 shows a detailed cross-section view of a model of the assembly. Photos of the assembled system can be found in Fig. 2.13 and in the Appendix.
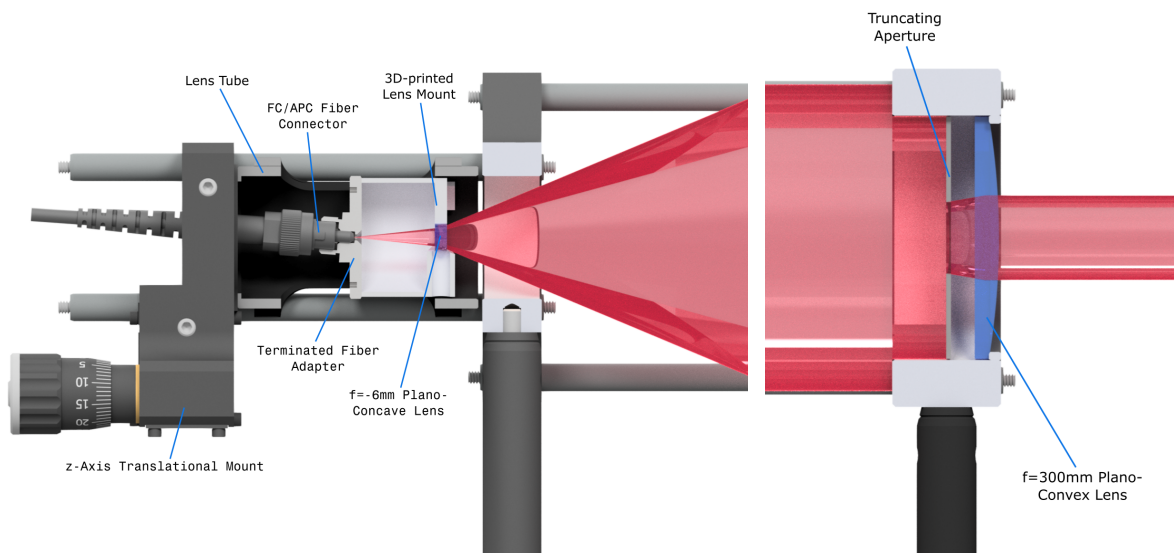
Figure 2.12: *Cross-section view of the CAD-model.*
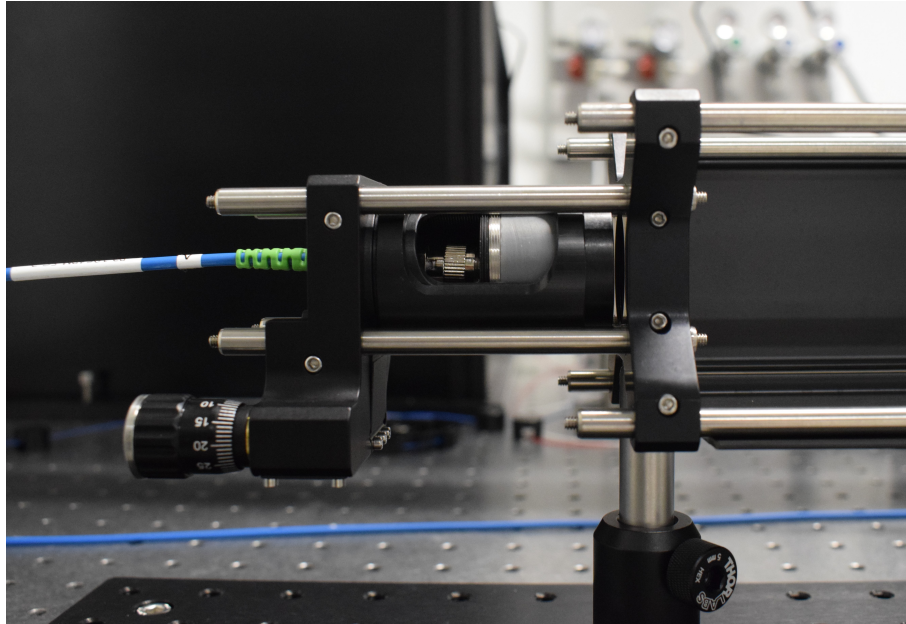
(a)
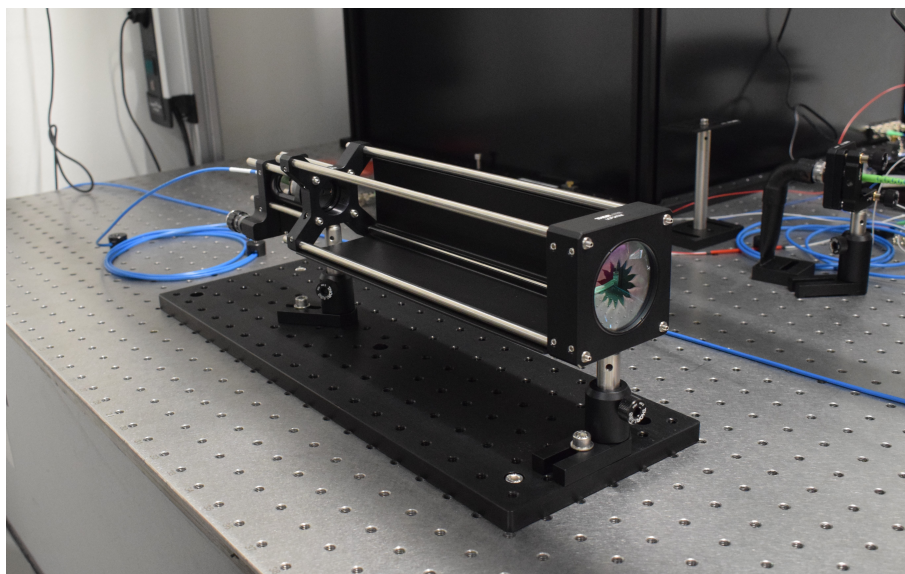
(b)

Figure 2.13: *Photos of the assembled system with two cage covers removed. (a) Lens tube with terminated fiber adapter and lens spacer. (b) Full assembly with apodizing aperture installed.*

3 Measurements and characterization

The following chapter contains measurements of the beam inside the optical system and of the produced flat-top beam. Measurements of the beam radius and intensity profile use a TaperCamD-LCM from DataRay equipped with an ND-1 filter since it has the largest effective sensor size among commercially available beam profilers. It uses a CMOS sensor with a $25 \times 25\,\mathrm{mm}$ active sensor area and a $12.5 \times 12.5\,\mathrm{\mu m}$ effective pixel size as stated in the specifications. DataRay's TaperCam series uses tapered fiber bundles to demagnify the image at the camera entrance and thus expand the imaging area of the sensor. Section 3.3 includes measurements of the beam's wavefront using a HASO3 128 GE2 wavefront sensor by Imagine Optic. This device measures the wavefront of a beam with an absolute accuracy of $\lambda/100 = 10.64\,\mathrm{nm}$ over its $14.6 \times 14.6\,\mathrm{mm}$ pupil. Data fits in the following chapter are created using the MATLAB Curve Fitting Toolbox. The axes in the transversal plane are defined such that the x-axis is horizontal and parallel to the optical table, while the y-axis is vertical and perpendicular to the optical table.

3.1 Beam exiting the waveguide

Parts of the design of the far-field generator are based on the assumption that light leaving a PM980-XP single-mode optical fiber can approximately be considered to be in the fundamental Gaussian mode. In section 2.3.1 the mode field diameter of the beam exiting the fiber is calculated to be $MFD = 7.14\,\mathrm{\mu m}$ using Marcuse's equation. That corresponds to a waist radius of $w(0) = 3.57\,\mathrm{\mu m}$ and a divergence angle of $\theta = 5.4°$. Measurement of the beam profile at different propagation distances indicates that the real divergence angle of the beam exiting the fiber is smaller.

To investigate this, the TaperCamD is positioned as closely to the fiber end as possible ($z \approx 6.5\,\mathrm{cm}$, this is restricted by the lens tube) and the beam profile is measured along the propagation axis in steps of $0.5\,\mathrm{cm}$ up to $z \approx 12.5\,\mathrm{cm}$, beyond which the beam diameter exceeds the sensor size. Fitting a Gaussian curve to the measured profiles and plotting the $1/e^2$ beam radius over the propagation distance yields Fig. 3.1b. Linear divergence can be assumed since $z \gg z_R$ and a linear fit to the evolving beam radius is used to determine the divergence angle $\theta = \arctan(0.07) \approx 4.0°$. According to eq. (2.8) that corresponds to a waist diameter of $MFD \approx 9.73\,\mathrm{\mu m}$, which differs noticeably from the

(a)   (b)
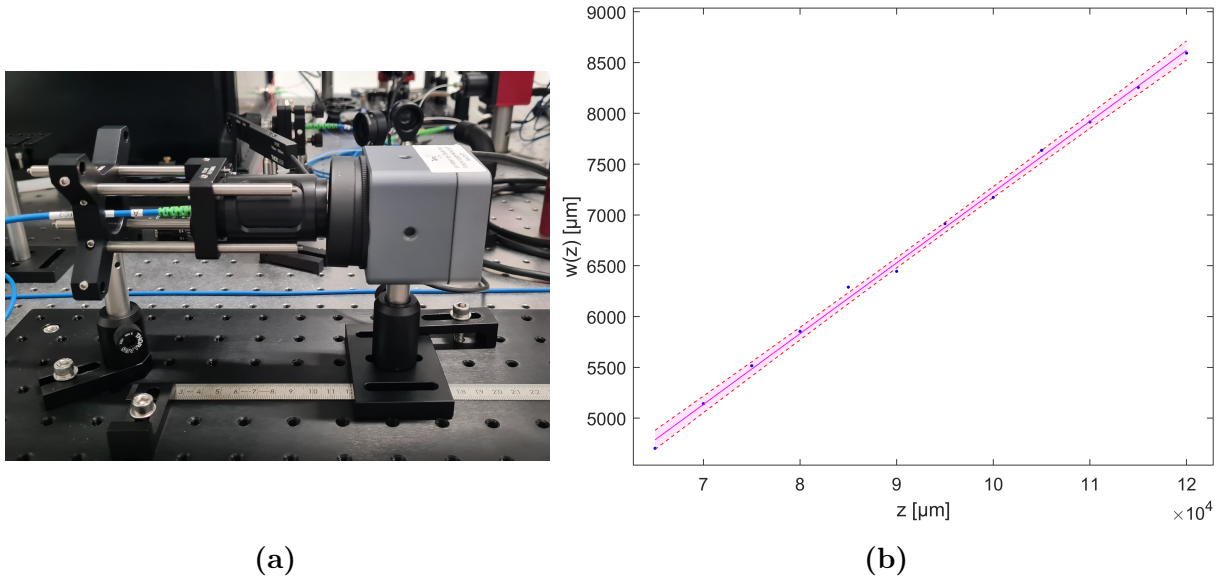
Figure 3.1: *(a) Experimental setup for divergence measurements. The lens tube is attached to the z-translational mount and contains the terminated fiber adapter. A centimeter rule is used to determine the distance between measuring points.*
(b) Evolving beam width behind a PM980-XP optical fiber. Includes measured data (blue) and a linear fit (red, incl. 95% confidence bounds). The fitted curve is $w(z) = 0.070z + 258$ with an R^2-value of approx. 0.998.

expected $MFD = 7.14 \, \mu m$. Using the 95% prediction bounds of the linear fit yields the interval $3.9° - 4.1°$ for the divergence angle and $9.43 - 10.06 \, \mu m$ for the MFD. Calculations of the divergence angle of the beam and the MFD are based on a linear fit rather than the measured radii and the corresponding propagation distance, because the distance between measuring points can be determined with higher accuracy than the distance from the emission surface. The assessment of the beam's divergence is based on the Gaussian curves that are fitted to the intensity profile in the x-direction. An analysis using profiles in the y-direction yields very similar results and is therefore not additionally included.

Furthermore, deviations from the Gaussian profile are visible in the beam exiting the fiber. These deviations are reproducible at different propagation distances and also after removing the ND-filter or using a different beam profiler (Beamage-4M from Gentec). The intensity profile along the horizontal axis of the beam (see Fig. 3.2) shows that the intensity distribution more closely resembles that of a Gaussian beam at longer propagation distances. The characteristic pattern depicted in Fig. 3.2 only occurs along the horizontal axis of the beam (perpendicular to the propagation axis and parallel to the optical table), the intensity profile along the y-axis shows only minor deviations from the ideal Gaussian profile.

Since the same intensity pattern occurs after changing the fiber and cleaning the emission surface, it is assumed that the deviations from an ideal Gaussian profile are inherent to
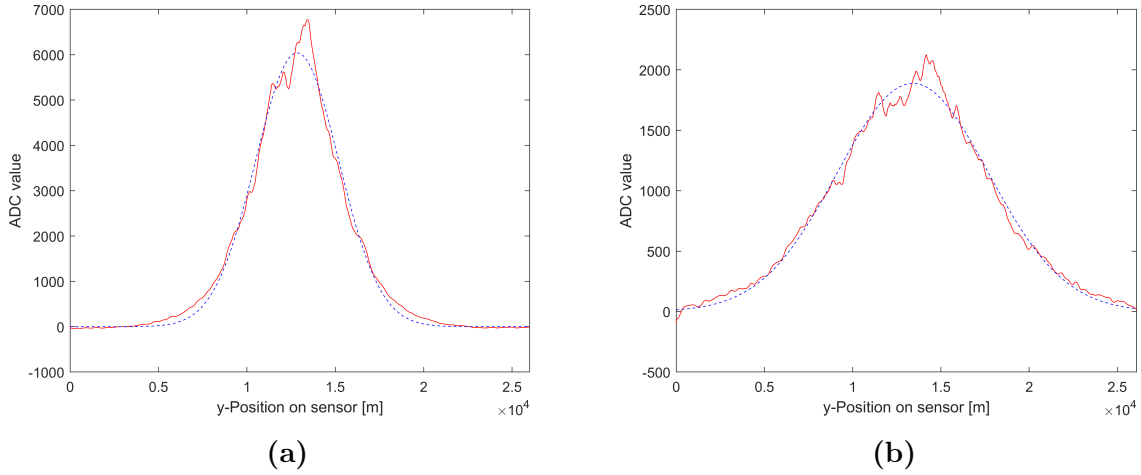
Figure 3.2: *Horizontal intensity profile and Gaussian fit to the beam exiting the PM980-XP optical fiber at (a) $z \approx 6.5\,\text{cm}$ and (b) $z \approx 12.5\,\text{cm}$.*
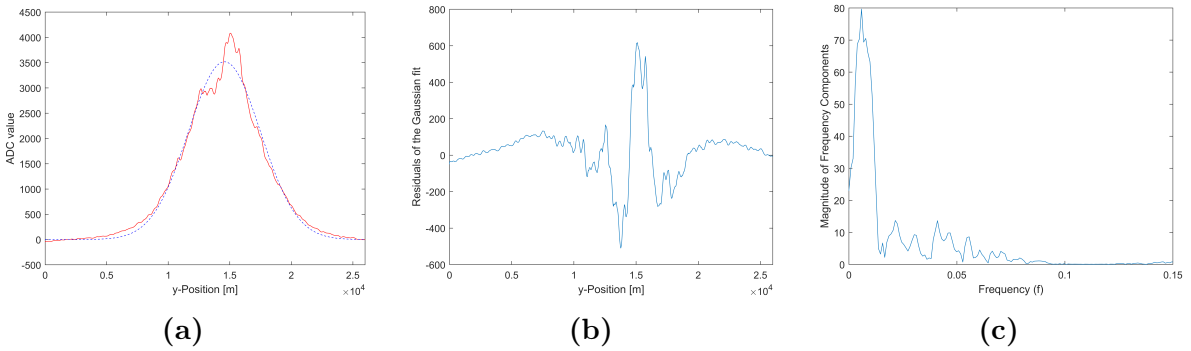
Figure 3.3: *Gaussian fit to the beam profile along the horizontal axis at $z \approx 9\,\text{cm}$. (a) Measured data and fitted curve. (b) Residuals of the fit. (c) Fourier transform of the residuals.*

the fiber type. Fig. 3.3a shows the intensity profile at $z \approx 9\,\text{cm}$ as well as the resulting Gaussian fit. The residuals of the fit can be seen in Fig. 3.3b and a Fourier transform of those residuals in Fig. 3.3c. A prominent spike in the Fourier transform suggests a periodic pattern in the observed deviations. This spike also appears at other propagation distances. A potential cause for this are the stress rods embedded in the cladding of polarization maintaining fibers. Here, the terminated fiber adapter and thus the fiber itself are oriented such that the slow axis of the fiber is parallel to the optical table, meaning the observed periodical deviations only occur along the slow axis, i.e. in the direction of the stress rods.

Neither the fact that the divergence angle is smaller than expected, nor the imperfect Gaussian intensity distribution in the beam can be addressed without using a different optical fiber, which is not available for this thesis. However, as Fig. 3.2 shows, a Gaussian intensity distribution is more closely matched with longer propagation, and the characteristic pattern is no longer visible behind the far-field generator at $z > 30\,\text{cm}$ (see section 3.3).

3.2   Divergence after the first lens

The beam divergence behind the plano-concave $f = -6\,\text{mm}$ lens is determined analogous to
the last section. The beam radius is measured at different positions, and a linear fit is used
to calculate the angle θ. By design, the divergence behind the lens is much larger, and the
beam width exceeds the sensor size after propagating only a few centimeters. Therefore,
the position of the lens tube is adjusted between measurements while the TaperCamD
remains stationary. Using the z-translational mount the position of the fiber's emission
surface and the first lens is accurately adjusted in $100\,\mu\text{m}$ increments. The beam profiler is
positioned as closely to the lens tube as possible at $z \approx 6.5\,\text{cm}$ or $4.5\,\text{cm}$ behind the plano
side of the lens. Fig. 3.4 shows the linear fit and an exemplary intensity profile along the
x-axis. The beam divergence is calculated based on the intensity profiles along the y-axis,
since those profiles more closely approximate a Gaussian distribution making the fits to
the measured data more reliable. The fitted function contains a constant term of $2508\,\mu\text{m}$
because the absolute distance to the beam waist is not significant for the divergence
calculation and is therefore approximated. As without the lens, the intensity distribution
is not perfectly Gaussian. The divergence angle is $\theta = \arctan(0.212) \approx 12.0°$ with the 95%
prediction bounds yielding the interval $10.3° - 13.7°$. This is again a smaller angle than
the expected $20.6°$ (see Fig. 2.6). According to eq. (2.10) that results in a beam radius at
$z = 30\,\text{cm}$ in the range of $w = 54 - 73\,\text{mm}$ instead of the planned $w \approx 113\,\text{mm}$. With the
beam's divergence angle being smaller than suggested by the simulations, a 1% intensity
variation over a beam with a $15\,\text{mm}$ diameter is not feasible (see eq. (2.5)). However, the
requirement can be met over a $10\,\text{mm}$ beam, assuming the divergence angle is on the upper
end of the 95% confidence interval of the fit with $\theta \geq 13.1°$ (see eq. (2.2)–(2.4)).

(a)   (b)
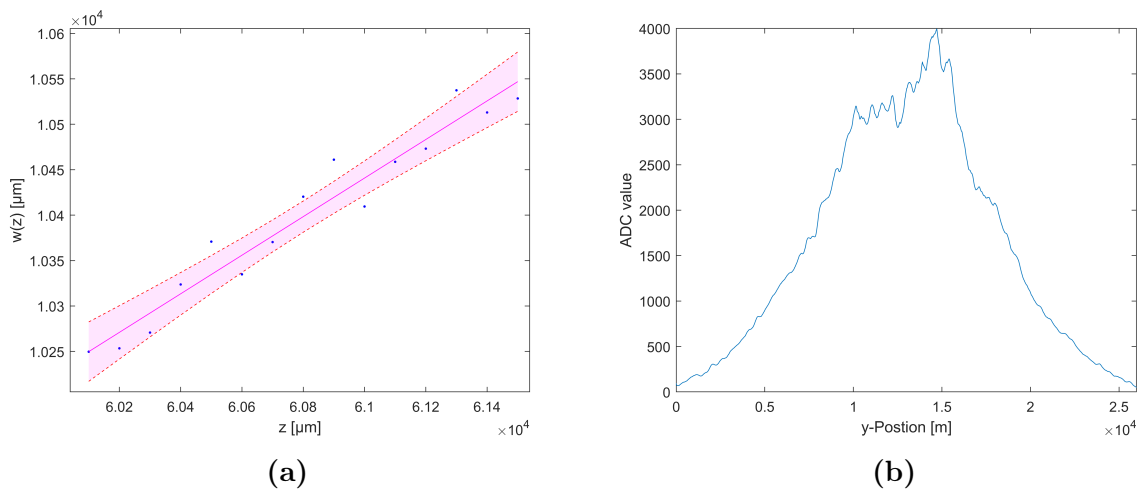
Figure 3.4: *(a) Evolving beam width behind the $f = -6\,\text{mm}$ lens. Includes measured
data (blue) and a linear fit (red, incl. 95% confidence bounds). The fitted curve is
$w(z) = 0.212z - 2508$ with an R^2-value of approx. 0.944 (b) Vertical intensity profile
behind the $f = -6\,\text{mm}$ lens at $z \approx 6.8\,\text{cm}$.*

3.3 Resulting flat-top beam

This section covers the characterization of the produced flat-top beam. The propagation of a beam truncated by a circular aperture is examined and compared to the development of one that has been truncated by an apodizing aperture.

3.3.1 Truncation with round aperture

According to the simulations conducted in section 2.3.3, a circular, hard aperture creates diffraction effects which lead to problematic ripples in the beam's intensity profile. To verify the assumption that an apodizing aperture is necessary, the propagation of a beam that has been truncated with a circular aperture is analyzed here. The aperture has a diameter of 15 mm and is manufactured using a 3D-printer. It is mounted directly before the collimating lens as pictured in Fig. 2.12. Figure 3.5b shows a photo of the aperture. The inner radius has a 45° chamfer to create a clearly defined aperture edge and avoid reflection from an internal surface. Because of that chamfer, the aperture is not completely opaque near the edge, as is visible in the backlit photo. That slight translucence does not have an apodizing effect since the light passing through the aperture edge is scattered by the material and cannot affect the interference patterns in the resulting beam.

The intensity measurements are again taken using a TaperCamD-LCM. In low-power measurements, patterns that are inherent to the camera are noticeable. The monochrome image of the intensity distribution in the beam behind the far-field generator with no lenses or aperture installed shows them as elliptical structures (see Fig. 3.5a). The pattern remains the same when the camera is shifted or rotated and cannot be removed via background subtraction or flat-field calibration. It is assumed that inhomogeneous responsivity of the CMOS sensor or artifacts from the demagnifying fiber-taper cause this pattern.


(a) (b)
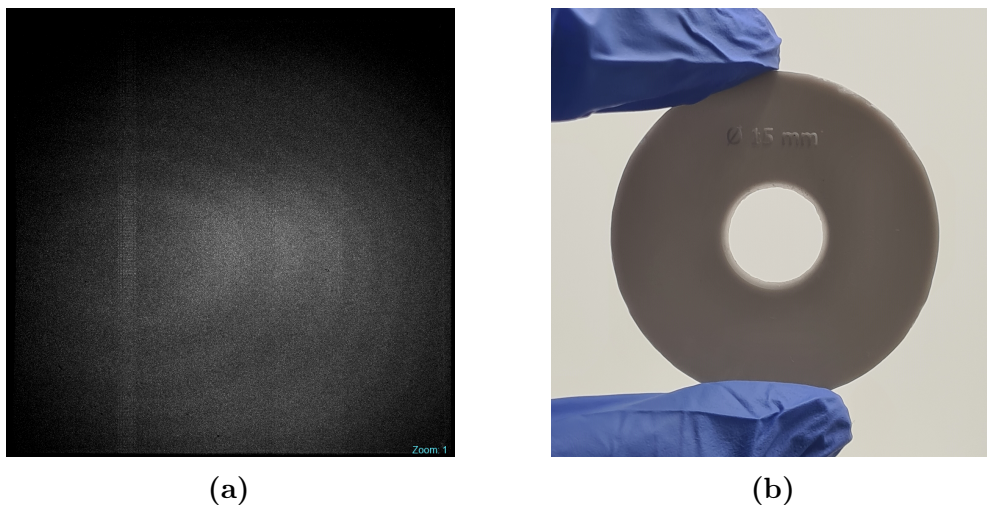
Figure 3.5: *(a) Intensity distribution in the beam behind the far-field generator with no lenses or aperture installed. Shown are the ADC values in a monochrome color-scale. (b) Photo of the 3D-printed round aperture.*

To examine the development of diffraction patterns in the beam, the intensity distribution is measured at $L = 10\,\text{cm}$, $L = 20\,\text{cm}$ and $L = 30\,\text{cm}$ behind the far-field generator. Additionally one measurement is taken as closely behind the collimating lens as possible at ($L \approx 2.5\,\text{cm}$). All measurements are taken with the circular aperture installed. A background subtraction is performed after moving the camera and each measurement consists of 20 averaged images. Fig. 3.6 shows the transversal intensity distributions. The false color images are normalized and a *0.2% triangular weighting smoothing function* (default value in the DataRay software) is applied to the intensity plots for noise reduction. All false color images show faint remnants of the elliptical pattern that is also visible in Fig. 3.5a. Overall, the profiles show a homogeneous intensity across the beam. Despite the applied smoothing function, high-frequency noise makes an exact examination of the flat-top uniformity impossible. It is highly unlikely that the plotted plateaus are a realistic representation of the intensity homogeneity in the beam, and it is assumed that the noise originates from the fiber-taper or other in-camera effects. Nonetheless, Fig. 3.6 shows the development of diffraction rings as close as 10 cm behind the far-field generator and a noticeably larger affected region after 20 and 30 cm, where approximately four maxima are distinguishable. Fig. 3.7a shows a plot of the intensity profile after 20 cm where the ADC values of 30 rows of pixels in the center of the beam are averaged. The diffraction ripples and the camera-inherent elliptical pattern are clearly visible. According to Fig. 3.7 a diameter of less than 11 mm is free from diffraction patterns, though similar to the intensity uniformity, the size of the undisturbed region in the beam is difficult to asses due to the noise in the measurements. The visible rings and the averaged intensity profile suggest that the results of the simulation in Fig. 2.9 are a valid representation of the real intensity profile.

The wavefront is measured to assess the flatness of the phase profile. During the setup of the far-field generator, the wavefront RoC calculated by the Imagine Optic WaveView software serves as an indicator for a well collimated system. After initial positioning, the z-translational mount can be used to adjust the position of the lens tube in sub-micrometer increments. It is important to note that at $\lambda/100$, the absolute accuracy of the sensor limits the collimation accuracy to some extent. Over the sensor's 14.6 mm pupil, a $\lambda/100 = 10.64\,\text{nm}$ wavefront sag corresponds to $RoC \approx 2500\,\text{m}$ (see eq. (2.1)) and a larger wavefront radius cannot be reliably resolved with the sensor. When the system is collimated to the best possible extent and no changes are made to the setup, the measured wavefront curvature at $L = 20\,\text{cm}$ fluctuates in the range of $RoC \approx 3 - 150\,\text{km}$. The wavefront is reconstructed using Zernike polynomials. To eliminate the tilt of the beam relative to the sensor, the first-order polynomials Z_1^{-1} and Z_1^1 are excluded. Fig. 3.7b shows a plot of the wavefront errors in the central 13 mm of the beam to exclude the maxima that occur at the edges. The peak-to-valley (PV) phase variation in the measured region is 262 nm or approx. $\lambda/4$ and the root-mean-squared (RMS) variation is $42\,\text{nm} \approx \lambda/25$. This is in the range of the wavefront errors that can be attributed to imperfect lens surfaces (see section 2.1.3).
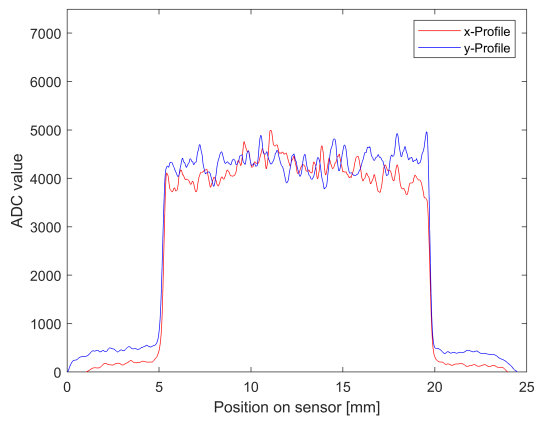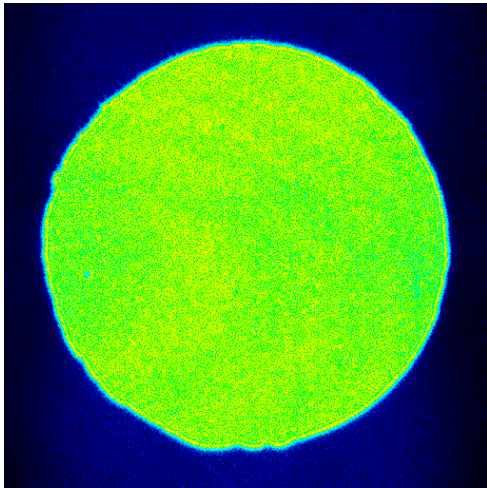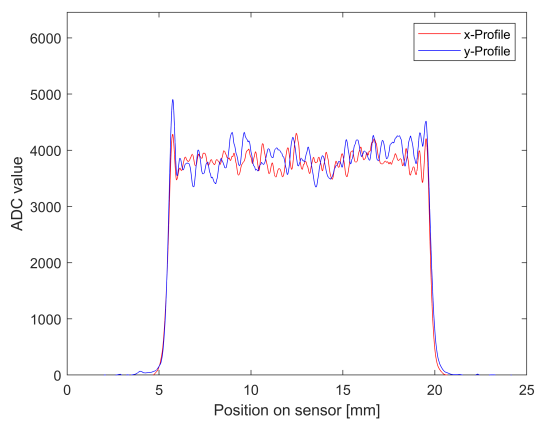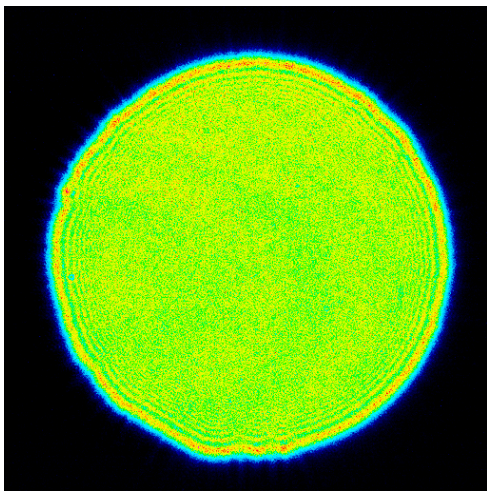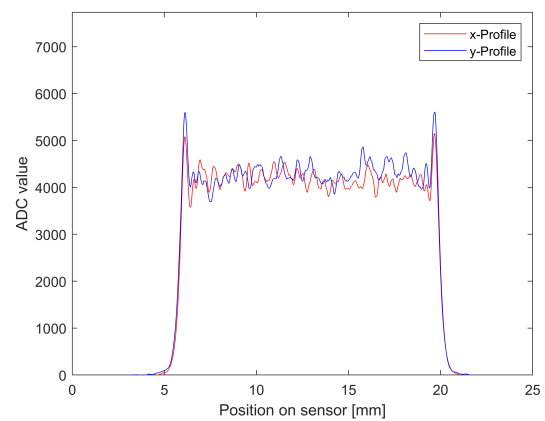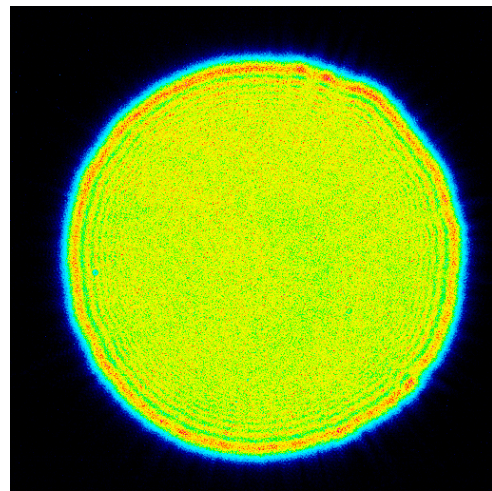
(a) *After* 2.5 cm
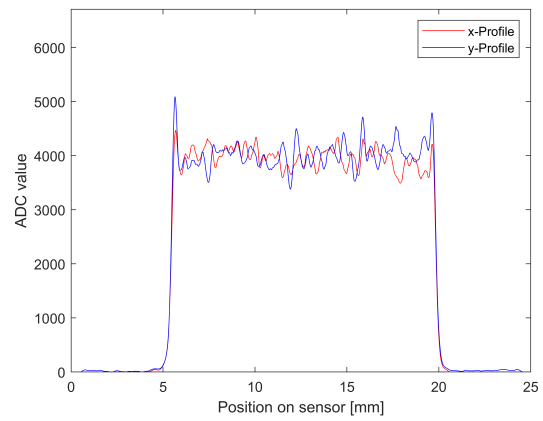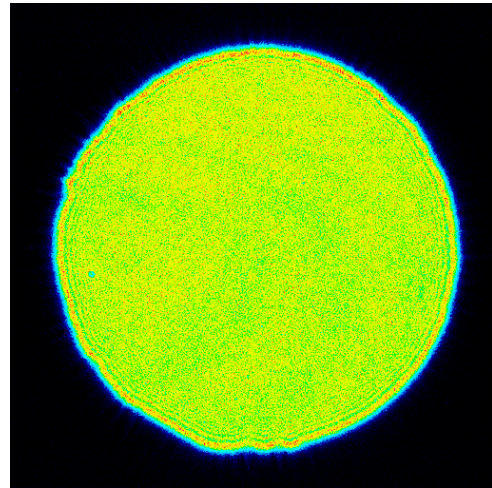
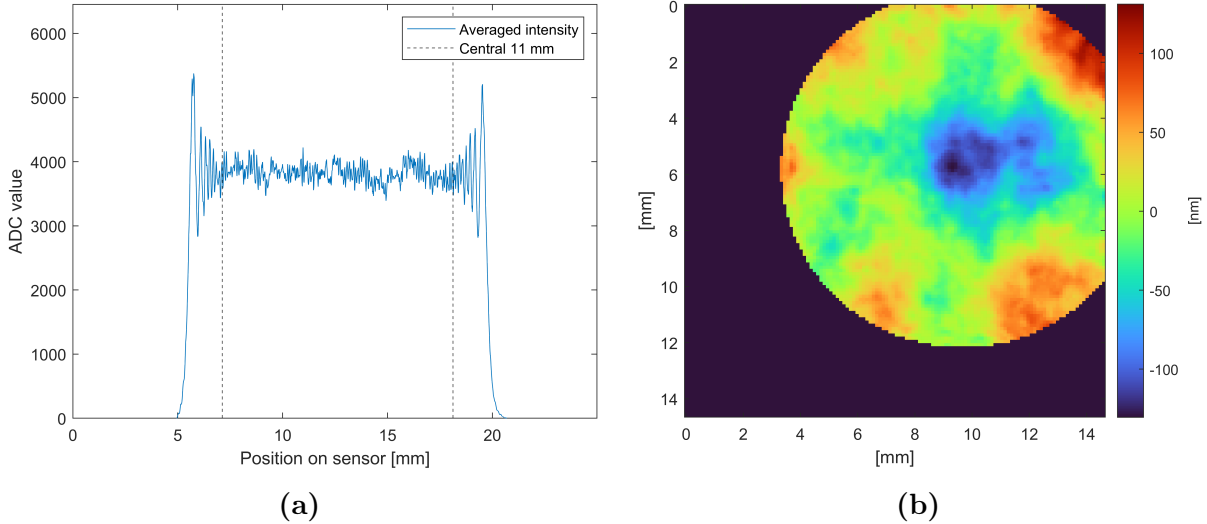

(b) *After* 10 cm

(c) *After* 20 cm

(d) *After* 30 cm

Figure 3.6: *On the previous page: Normalized intensity distribution in the beam behind a circular truncating aperture. The figures show a false color image of the intensity distribution and a plot of the intensity profile along the x- and y-axis through the center of the beam.*

(a)   (b)

Figure 3.7: *(a) Averaged intensity profile at $L = 20$ cm. The plot shows the average of 30 pixel rows in the x-direction at the center of the beam. (b) Map of the deviation from an ideal wavefront [nm] behind a round aperture. The measurement is taken at $L = 20$ cm and the central circle with a diameter of 13 mm is displayed here. Tilt in the x- and y-directions is removed by the software (see text).*

3.3.2   Truncation with apodizing aperture

With an apodizing aperture the visible effects of diffraction at the aperture edge can be significantly reduced. This section characterizes the resulting beam after passing through an apodizing truncating aperture that is positioned immediately before the collimating lens. The aperture geometry is as described in section 2.3.3. The aperture is 3D-printed and has a clear diameter of 16.2 mm (referring to the circle inscribed in the petal-tips). Similar to the circular aperture, it has a 45° chamfer on the internal edge to achieve clearly defined aperture edges and petal-tips. Fig. 3.8 shows a photo of the apodizing aperture and a detailed view of the petals.

The figures in 3.9 show that due to the unique edge geometry of the aperture, the diffraction patterns extend over a smaller region of the beam. The measurements are performed analogously to section 3.3.1. Each false color image is averaged over 20 measurements and the *0.2% smoothing function* is applied to the profile plots by the DataRay software. Immediately behind the collimating lens, no diffraction effects are visible but the profiles along both axes are curved with an intensity maximum at the center (see Fig. 3.9a). The maximum is more prominent than can be attributed to the overall Gaussian intensity profile of the beam. According to eq. (2.2)–(2.4), a beam width as calculated in section 3.2 causes an intensity drop of 2.4%–4.5% between the propagation axis and the petal tips.

(a)   **(b)**

Figure 3.8: *(a) Top view of two apodizing apertures with* 16.2 *and* 18.1 mm *clear aperture. (b) Detailed view of the petal-tips of an apodized aperture.*

After 10, 20 and 30 cm the measured profiles show no curve and diffraction patterns become visible in the petals. As indicated by the simulation results (see Fig. 2.10), intensity ripples starting at the petal tips affect part of the central beam area. The false color images also show the same elliptical structures as Fig. 3.5a and 3.7a, though they are most easily identifiable at $L = 10$ cm due to the normalized color-scale. In the plotted intensity profiles, neither of those features is clearly identifiable but the averaged intensity profile across 20 columns of pixels (see Fig. 3.10a) shows both: the ripples from diffraction at the aperture edge and the sensor-inherent pattern. Unlike in the previous section, the data is averaged across multiple columns in the y-direction because the aperture is oriented in such a way that the vertical crosshair lines up with the central petal tips (see Fig. 3.9). Due to slight rotational misalignment of the aperture, the crosshairs only intercept the petal tip at one edge of the beam and Fig. 3.10a only shows ripples on the left side of the profile. Again, the measurements include too much noise to reliably analyze the intensity homogeneity across the flat-top plateau. Nonetheless, no intensity drop towards the beam edge is visible at $L = 20$ cm and, except for $L = 2.5$ cm, all measurements agree with the simulation results in Fig. 2.10. The intensity at the center of the beam is measured to be approximately 66 mW/m^2 using a Thorlabs PM100D power meter.

With the system collimated as accurately as possible using the HASO3 sensor, the wavefront is measured over the central 15 mm of the beam (see Fig. 3.11). The PV wavefront error in that region is 146 nm $\approx \lambda/7$ and the RMS variation is 23 nm $\approx \lambda/46$. The present phase variation can again be attributed to irregularities in the lens surfaces. Analogous to the previous section, reconstruction of the wavefront using the WaveView software and Zernike polynomials confirms that the quality of the collimation is limited by the accuracy of the sensor. In the collimated configuration, the RoC fluctuates in the kilometer-range with no changes made to the setup.
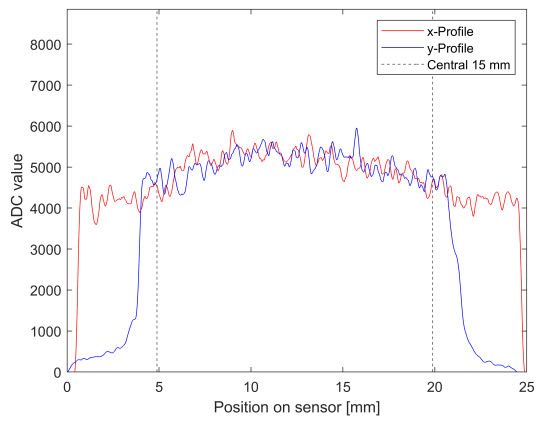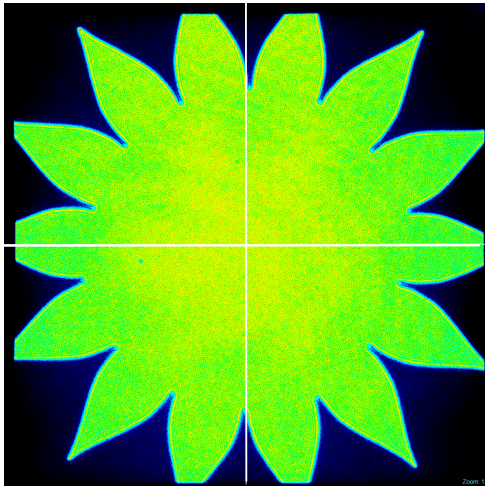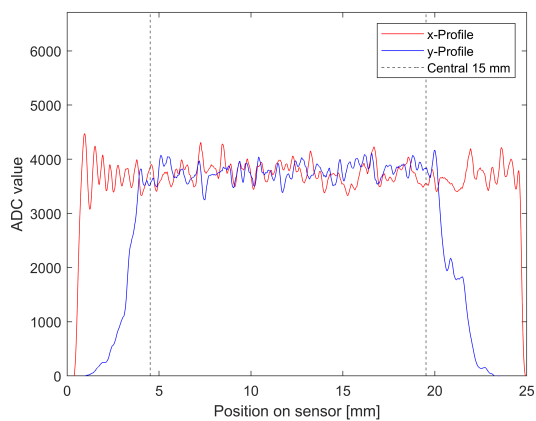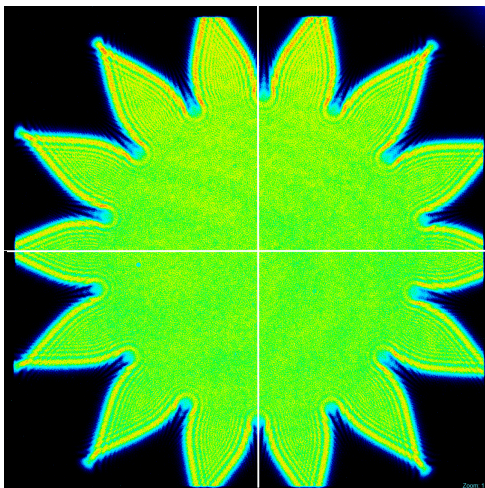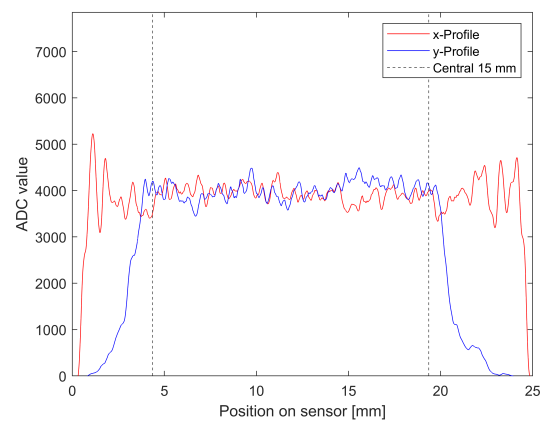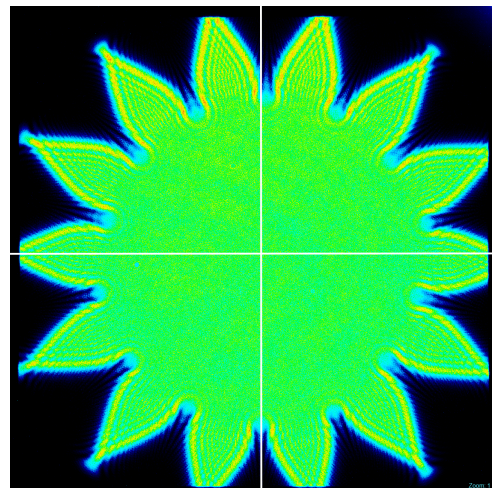
(a) *After* 2.5 cm
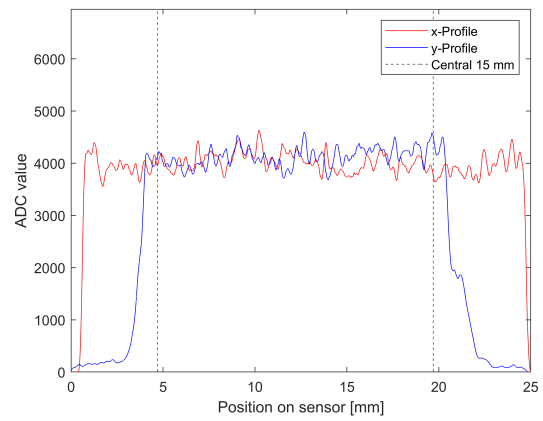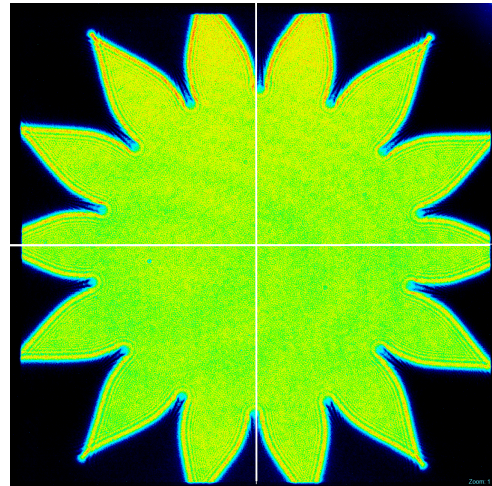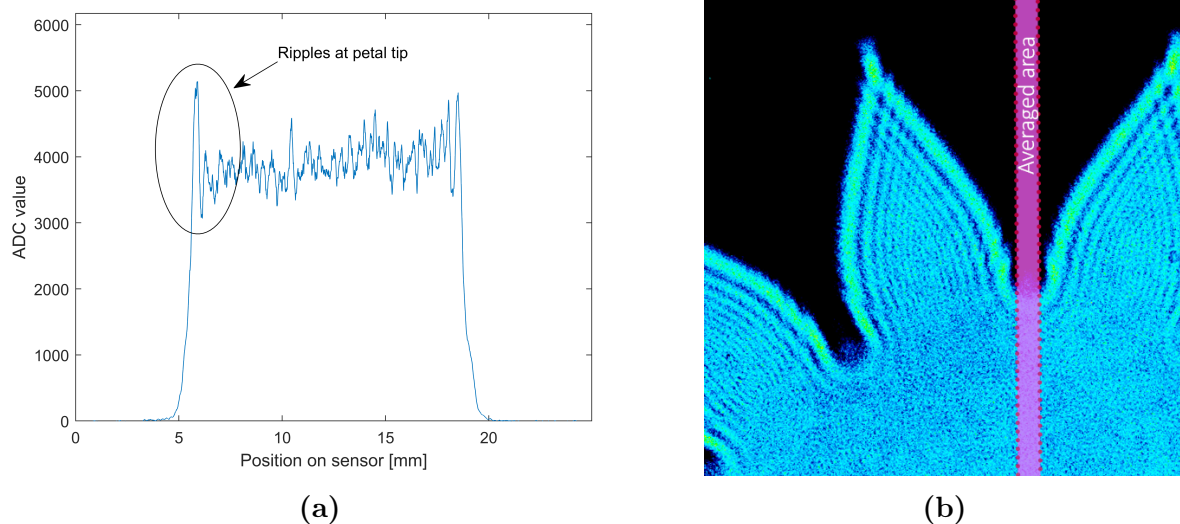


(b) *After* 10 cm

(c) *After* 20 cm

(d) *After* 30 cm

Figure 3.9: *On the previous page: Normalized intensity distribution in the beam behind an apodizing truncating aperture with 16.2 mm of clear aperture. The figures show a false color image of the intensity distribution and a plot of the intensity profile along the x- and y-axis through the center of the beam.*

(a)

(b)

Figure 3.10: *(a) Averaged intensity profile at L = 20 cm. The plot shows the average of 30 pixel columns in the y-direction at the position of a petal tip. (b) Detailed view of the intensity distribution at the beam edge (not normalized for better contrast).*
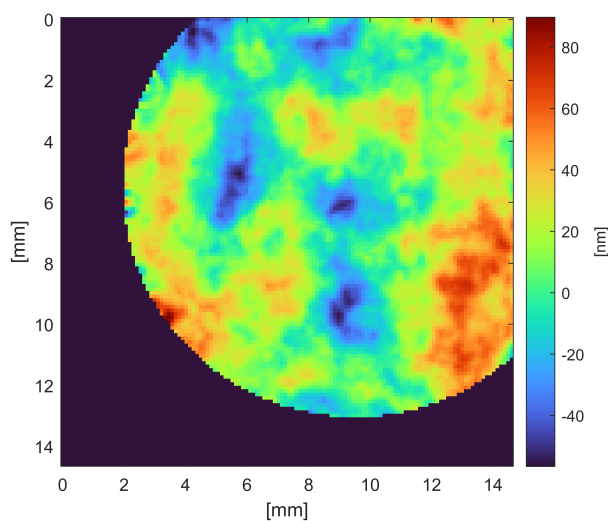
Figure 3.11: *Map of the deviation from an ideal wavefront [nm] behind an apodizing aperture. The measurement is taken at L = 20 cm and the central circle with a diameter of 15 mm is displayed here. Tilt in the x- and y-directions is removed by the software (see text).*

4 Discussion and outlook

4.1 Discussion of the results

The aim of this thesis was the development of an optical system that can provide an RX-beam for laser interferometers and to evaluate its performance. The final design incorporates the results of previous work in the field to create an integrated system that reproduces the properties of a laser beam in the far-field. Both, the beam truncated by a circular aperture and the one truncated by an apodizing aperture show distinct flat-top characteristics. With a circular aperture installed in the system, diffraction rings develop as indicated by the simulations. The expected intensity ripple fluctuations in the center of the beam behind a circular aperture are not visible in the measurements because the affected region spans only a few pixels on the sensor (see section 2.3.3) and cannot be resolved here. Additionally, it is possible that the effect is attenuated due to the imperfect circular symmetry of the 3D-printed aperture (see Fig. 3.5b).

With an aperture whose edge geometry approximates hyper-Gaussian apodization, a larger cross-sectional area of the beam remains free from visible and relevant diffraction patterns. Such an aperture also avoids the possibility of intensity fluctuations in the center of the beam. Analysis of the measured intensity profiles shows more stable propagation of the beam behind an apodizing aperture.

By adjusting the distance between the lens tube and the collimating lens, the resulting beam can be collimated to achieve a radius of wavefront curvature larger than $2500\,\mathrm{m}$, limited by the available wavefront sensor. The RMS wavefront error in the beam behind the apodizing aperture is $\lambda/46$ with a PV value of $\lambda/7$. In this range, the wavefront homogeneity can only be improved by using higher quality lenses.

The investigation of the beam divergence shows a smaller than expected divergence angle after exiting the optical fiber as well as behind behind the $f = -6\,\mathrm{mm}$ lens. These results disagree with the calculations performed in section 2.3.1 regarding the mode field diameter of the initial beam. Measurements of the beam's profile inside the optical system support the assumption of an overall Gaussian intensity distribution in the initial beam, though the deviation from an ideal Gaussian profile is stronger than expected.

The intensity homogeneity across the flat-top plateau cannot be examined to the desired level with the available equipment due to sensor-inherent patterns and noise in the measurements. In the target plane, $20\,\mathrm{cm}$ behind the far-field generator, no intensity drop-off towards the edges of the beam is visible. Based on the measured beam divergence behind the plano-

concave lens, an effective beam radius of $w = 54$–$73\,\text{mm}$ and thus an intensity variation of $0.94\,\% - 1.72\,\%$ is expected across a diameter of $10\,\text{mm}$ at the center of the beam. Across an RX-aperture of an optical bench with a diameter of $8\,\text{mm}$, this corresponds to an intensity inhomogeneity of $0.60\,\% - 1.10\,\%$. The measured profiles generally agree with the simulation results and suggest that diffraction effects from an apodizing aperture have a negligible impact on the intensity homogeneity in the central region. Different means of measuring the intensity distribution are necessary in order to reliably examine the homogeneity of the resulting beam with the desired accuracy.

4.2   Conclusion and future directions

The results in section 3.3 demonstrate that the developed system successfully produces a flat-top beam with a quasi-flat wavefront. The diameter of the flat-top region of the beam is approximately $15\,\text{mm}$, although the results do not indicate a homogeneity of $\geq 99\%$ over the complete intensity plateau. Based on the experimental results, it cannot be confirmed to what extend the homogeneity requirement is met over a smaller diameter. The system can be collimated to a point where the wavefront radius of curvature causes a phase variation $\leq \lambda/100$. The results presented here refer to the target plane at $L = 20\,\text{cm}$, though the degree of collimation and the development of the intensity distribution suggest a usable flat-top region of at least $30\,\text{cm}$. Being mounted on a $15 \times 45\,\text{cm}$ optical breadboard, the system meets the requirements of being transportable and having a footprint smaller than $50\,\text{cm}$.

The system developed in the context of this thesis achieves the objective of imitating a laser beam in the far-field. The key characteristics of an RX-beam originating from a distant spacecraft are replicated in the beam emitted by the far-field generator. The far-field generator also has the potential for further enhancement. If the phase or intensity profiles of the generated beam prove to be inadequate for future applications, single components can be exchanged without compromising the functionality of the system. To achieve a more homogeneous phase profile, higher-quality lenses with the same focal lengths can be used to introduce smaller wavefront errors. Additionally, the use of aspheric lenses can eliminate spherical aberrations in future iterations of the system. Substituting the optical fiber for one that has a mode field diameter of approximately $7\,\mu\text{m}$ or less when operating at $1064\,\text{nm}$ would ensure the required intensity variation of $\leq 1\%$ over the truncating aperture by providing a beam with a larger divergence angle. Furthermore, the adherence to a Gaussian intensity profile can be enhanced by utilizing an optical fiber that is optimized for free-space coupling. A revised version of the apodizing truncating aperture can be manufactured using a more precise method to achieve very fine petal-tips or pursue a different apodization method to further inhibit the development of diffraction patterns in the beam. Future work should focus on quantifying the intensity homogeneity across the flat-top region and exploring the practical applications of the system as optical ground support equipment.

Bibliography

[1] H. Drewes and J. Ádám, "The International Association of Geodesy: From an ideal sphere to an irregular body subjected to global change", *History of Geo- and Space Sciences*, vol. 10, no. 1, pp. 151–161, Apr. 2019, ISSN: 2190-5029. DOI: 10.5194/hgss-10-151-2019.

[2] S. Jin, T. van Dam, and S. Wdowinski, "Observing and understanding the Earth system variations from space geodesy", *Journal of Geodynamics*, vol. 72, pp. 1–10, Dec. 2013, ISSN: 0264-3707. DOI: 10.1016/j.jog.2013.08.001.

[3] M. Drinkwater, R. Floberghagen, R. Haagmans, D. Muzi, and A. Popescu, "GOCE: ESA's first earth explorer core mission", *Earth gravity field from space - from sensors to Earth sciences. In the Space Sciences Series of ISSI*, vol. 18, G. Beutler, M. R. Drinkwater, R. Rummel, and R. von Steiger, Eds., pp. 419–432, 2003.

[4] B. D. Tapley, S. Bettadpur, M. Watkins, and C. Reigber, "The gravity recovery and climate experiment: Mission overview and early results", *Geophysical Research Letters*, vol. 31, no. 9, May 2004, ISSN: 1944-8007. DOI: 10.1029/2004GL019920.

[5] S. Kayali, P. Morton, and M. Gross, "International challenges of GRACE Follow-On", in *2017 IEEE Aerospace Conference*, IEEE, Mar. 2017. DOI: 10.1109/aero.2017.7943615.

[6] B. S. Sheard, G. Heinzel, K. Danzmann, D. A. Shaddock, W. M. Klipstein, and W. M. Folkner, "Intersatellite laser ranging instrument for the GRACE follow-on mission", *Journal of Geodesy*, vol. 86, no. 12, pp. 1083–1095, May 2012, ISSN: 1432-1394. DOI: 10.1007/s00190-012-0566-3.

[7] K. Abich, A. Abramovici, B. Amparan, *et al.*, "In-Orbit Performance of the GRACE Follow-on Laser Ranging Interferometer", *Phys. Rev. Lett.*, vol. 123, p. 031 101, 3 Jul. 2019. DOI: 10.1103/PhysRevLett.123.031101.

[8] F. W. Landerer, F. M. Flechtner, H. Save, *et al.*, "Extending the global mass change data record: GRACE Follow-On instrument and science data performance", *Geophysical Research Letters*, vol. 47, no. 12, Jun. 2020, ISSN: 1944-8007. DOI: 10.1029/2020gl088306.

[9] P. L. Bender, D. N. Wiese, and R. S. Nerem, "A possible dual-GRACE mission with 90 degree and 63 degree inclination orbits", in *Proceedings of the 3rd International Symposium on Formation Flying, Missions and Technologies*, ESA/ESTEC Noordwijk, 2008, pp. 1–6.

[10] B. Elsaka, J.-C. Raimondo, P. Brieden, *et al.*, "Comparing seven candidate mission configurations for temporal gravity field retrieval through full-scale numerical simulation", *Journal of Geodesy*, vol. 88, no. 1, pp. 31–43, Nov. 2013, ISSN: 1432-1394. DOI: 10.1007/s00190-013-0665-9.

[11] L. Massotti, C. Siemes, G. March, R. Haagmans, and P. Silvestrin, "Next Generation Gravity Mission Elements of the Mass Change and Geoscience International Constellation: from orbit selection to instrument and mission design", *Remote Sensing*, vol. 13, no. 19, p. 3935, Oct. 2021, ISSN: 2072-4292. DOI: 10.3390/rs13193935.

[12] Deutsches Zentrum für Luft- und Raumfahrt, *GRACE-C – German-US-American environmental mission has been extended*, Accessed Apr. 26, 2024. [Online]. Available: https://www.dlr.de/en/latest/news/2024/grace-c-german-us-american-environmental-mission-has-been-extended.

[13] T. G. Huntington, "Evidence for intensification of the global water cycle: Review and synthesis", *Journal of Hydrology*, vol. 319, no. 1–4, pp. 83–95, Mar. 2006, ISSN: 0022-1694. DOI: 10.1016/j.jhydrol.2005.07.003.

[14] I. Daras, G. March, R. Pail, *et al.*, "Mass-change And Geosciences International Constellation (MAGIC) expected impact on science and applications", *Geophysical Journal International*, vol. 236, no. 3, pp. 1288–1308, Dec. 2023, ISSN: 1365-246X. DOI: 10.1093/gji/ggad472.

[15] I. Daras, Ed., *Next Generation Gravity Mission (NGGM) mission requirements document, issue 1.0*. Earth and Mission Science Division, European Space Agency, Sep. 2023. DOI: 10.5270/esa.nggm-mrd.2023-09-v1.0.

[16] A. Koch, "Link acquisition and optimization for intersatellite laser interferometry", Ph.D. dissertation, Leibniz Universität Hannover, 2020. DOI: 10.15488/9799.

[17] F. M. Dickey and T. E. Lizotte, Eds., *Laser beam shaping applications*, 2nd ed., Boca Raton: CRC Press, Dec. 2016, 442 pp., ISBN: 9781315371306. DOI: 10.1201/9781315371306.

[18] F. M. Dickey, Ed., *Laser beam shaping: Theory and techniques, second edition*, 2nd ed., Boca Raton: CRC Press, Jan. 2017, 590 pp., ISBN: 9781315216164. DOI: 10.1201/b17140.

[19] X. Zhu, A. Schülzgen, H. Li, H. Wei, J. V. Moloney, and N. Peyghambarian, "Coherent beam transformations using multimode waveguides", *Optics Express*, vol. 18, no. 7, pp. 7506–7520, Mar. 2010, ISSN: 1094-4087. DOI: 10.1364/OE.18.007506.

[20] J. A. Hoffnagle and C. M. Jefferson, "Design and performance of a refractive optical system that converts a Gaussian to a flattop beam", *Applied Optics*, vol. 39, no. 30, p. 5488, Oct. 2000, ISSN: 1539-4522. DOI: `10.1364/ao.39.005488`.

[21] A. Laskin, "Achromatic optical system for beam shaping", U.S. Patent 8 023 206, 2011.

[22] A. Laskin and V. Laskin, "Beam shaping to generate uniform laser light sheet and linear laser spots", in *Laser Beam Shaping XIV*, A. Forbes and T. E. Lizotte, Eds., SPIE, Sep. 2013. DOI: `10.1117/12.2021459`.

[23] A. Laskin and V. Laskin, "Beam shaping optics to improve holographic and interferometric nanomanufacturing techniques paper n405", ICALEO 2012, Tech. Rep., 2012.

[24] C. Baune, "Design, implementation and characterization of atelescope simulator for the LISA optical bench", M.S. thesis, Leibniz Universität Hannover, Sep. 2009.

[25] H. Lee, J. Park, and K. Oh, "Recent progress in all-fiber non-Gaussian optical beam shaping technologies", *Journal of Lightwave Technology*, vol. 37, no. 11, pp. 2590–2597, Jun. 2019, ISSN: 1558-2213. DOI: `10.1109/jlt.2018.2878490`.

[26] AdlOptica, *πShaper 6_6 series*, Accessed May 2, 2024. [Online]. Available: `https://pishaper.com/shaper.html`.

[27] G. Fernández Barranco, M. Tröbs, V. Müller, O. Gerberding, F. Seifert, and G. Heinzel, "Spatially resolved photodiode response for simulating precise interferometers", *Applied Optics*, vol. 55, p. 6688, Aug. 2016. DOI: `10.1364/AO.55.006688`.

[28] A. E. Siegman, *Lasers*. Mill Valley, California: University Science Books, 1986, 1283 pp., Literaturangaben, ISBN: 0935702113.

[29] I. Sizova, T. Moskalev, and L. Mikheev, "Laser beam shaping with circular serrated apertures. i. spatial filtering", *Applied Optics*, vol. 58, no. 18, p. 4905, Jun. 2019, ISSN: 2155-3165. DOI: `10.1364/ao.58.004905`.

[30] I. Sizova, T. Moskalev, and L. Mikheev, "Laser beam shaping with circular serrated apertures. II. Theory of the beam profile formation", *Applied Optics*, vol. 58, no. 18, p. 4910, Jun. 2019, ISSN: 2155-3165. DOI: `10.1364/ao.58.004910`.

[31] I. Sizova, T. Moskalev, and D. Stavrovskii, "Correction of shape distortions in laser beams apodized with circular serrated apertures", *Applied Optics*, vol. 60, no. 16, p. 4861, Jun. 2021, ISSN: 2155-3165. DOI: `10.1364/ao.423334`.

[32] M. T. YUrevich and M. L. Dmitrievich, "Apodizator of laser beam", Russian Federation Patent 2587694 C1, Jun. 20, 2016.

[33] J. Degallaix, "OSCAR: A MATLAB based package to simulate realistic optical cavities", *SoftwareX*, vol. 12, p. 100 587, Jul. 2020. DOI: `10.1016/j.softx.2020.100587`.

[34] D. Marcuse, "Loss analysis of single-mode fiber splices", *Bell System Technical Journal*, vol. 56, no. 5, pp. 703–718, May 1977, ISSN: 0005-8580. DOI: `10.1002/j.1538-7305.1977.tb00534.x`.

[35] A. W. Snyder, *Optical waveguide theory* (Science paperbacks 190), [Reprint], J. D. Love, Ed. Boston: Kluwer Academic Publishers, 2000, 734 pp., ISBN: 0412242508.

[36] W. Cash, "Detection of earth-like planets around nearby stars using a petal-shaped occulter", *Nature*, vol. 442, no. 7098, pp. 51–53, Jul. 2006, ISSN: 1476-4687. DOI: `10.1038/nature04930`.

[37] W. Cash, "Analytic modeling of starshades", *The Astrophysical Journal*, vol. 738, no. 1, p. 76, Aug. 2011, ISSN: 1538-4357. DOI: `10.1088/0004-637x/738/1/76`.

[38] M. D. Lieser, "LISA optical bench development: Experimental investigation of tilt-to-length coupling for a spaceborne gravitational wave detector", Ph.D. dissertation, Leibniz U., Hannover, 2017. DOI: `10.15488/9016`.

[39] M. Chwalla, K. Danzmann, G. Fernández Barranco, *et al.*, "Design and construction of an optical test bed for LISA imaging systems and tilt-to-length coupling", *Classical and Quantum Gravity*, vol. 33, no. 24, p. 245 015, Nov. 2016, ISSN: 1361-6382. DOI: `10.1088/0264-9381/33/24/245015`.

[40] M. Chwalla, K. Danzmann, M. D. Álvarez, *et al.*, "Optical suppression of tilt-to-length coupling in the LISA long-arm interferometer", *Physical Review Applied*, vol. 14, no. 1, p. 014 030, Jul. 2020, ISSN: 2331-7019. DOI: `10.1103/physrevapplied.14.014030`.

[41] "Form 3 dimensional accuracy report", Formlabs, Tech. Rep., May 2021.

A Small-lens adapter

The small-lens adapter is necessary to center the LC2969-C plano-concave lens in a SM1 lens tube. Commercially available adapters are not suited because most use a lip to retain the lens and thus further limit its 6 mm clear aperture diameter. Alternatives that instead use a set-screw to secure the lens are not available with the necessary 1 " outer diameter.

To achieve its primary function, the adapter is designed with an outer diameter of exactly 1 " or 25.4 mm and an inner diameter of 6.1 mm to allow for installation and removal of the lens without damaging it. Furthermore, the component serves as a spacer to accurately control the distance between the lens and the terminated fiber adapter. Therefore, the adapter features a tubular section with a thickness of 1 mm, ensuring that the front face of the adapter is positioned 19.8 mm from the optical fiber's emission surface. A through-hole at the adapter's end contains an M3 thread insert and the lens is secured using a nylon-tipped set-screw. The end face features four contact points for an SM1 retaining ring and slots to facilitate manufacturing with a resin 3D-printer.

(a)   **(b)**

Figure A.1: *(a) CAD-model of the lens adapter. (b) Half-section view of the model, showing the placement of the lens and the thread insert.*

B OSCAR: An FFT MATLAB Add-On

B.1 About Oscar

OSCAR is a Fast Fourier Transform (FFT) code that allows the simulation of electromagnetic field propagation in MATLAB. OSCAR was developed by Jerome Degallaix and originally intended for the analysis of Fabry-Perot cavities.

Electromagnetic fields are handled as two-dimensional arrays that contain the electric field vectors across some area of a plane in complex notation. One instance of the *E_field* class contains the field vectors that correspond to a two-dimensional area of a field with specified dimensions and resolution. To simulate the interaction of electromagnetic waves with optical components or free-space propagation, custom functions are applied to the *E_field* object. The resulting *E_field* is calculated via FFT and output by the function. Two custom functions that build on the OSCAR add-on were developed during the design-phase of this thesis. This appendix briefly explains the motivation and functionality of these functions.

B.2 The Transmit_Pinhole function

The *Transmit_Pinhole* function was created to investigate propagation through very small apertures using OSCAR. Using the regular *Transmit_Aperture* function that is part of the OSCAR add-on becomes problematic when the aperture diameter is of the same order as the effective pixel size of the input *E_field* object. Inside the *Transmit_Pinhole* function, a new, resized *E_field* object is created using the beam parameters of the input field. Using OSCAR's *Fit_TEM00* function the beam radius and the wavefront radius of curvature of the simulated beam are calculated. The new *E_field* object is defined as having an effective edge length of three times the aperture diameter, and containing the complex field vectors that describe the same Gaussian beam as the input field. The newly defined *E_field* is then input into OSCAR's *Transmit_Aperture* function. The result is an *E_field* object containing the field vectors that represent a beam which has propagated through a pinhole. By defining a resized instance of *E_field*, the aperture diameter is represented by enough pixels to yield a reliable result. It should be noted that the function assumes the incident beam to have an ideal Gaussian intensity distribution, so any aberrations present in the input field are not transferred to the output.

B.3   The E_Cross function

The *E_ Cross* function was created to provide an easy way to compare the intensity profiles at different propagation distances and behind different apertures. The function plots the intensity profile over the center of the area associated to an *E_ field* object and was also used to create the intensity profile plots in section 2.3.3. Input arguments for the function are an *E_ field* object and an integer to specify the desired width of the output plot. The central row of the array containing the complex field vectors is extracted from the input field and squared to create a one-dimensional array of intensity values. Electromagnetic fields that are calculated using OSCAR have an amplitude in the unconventional unit $\sqrt{(\text{W})}$/m. Therefore, intensity values are easily calculated by squaring the absolute value of the contents of an *E_ field* object. As stated in 2.3.1, to obtain the amplitude in the standard V/m, the absolute values must be multiplied by $\sqrt{2\eta}$, where η is the free-space impedance.

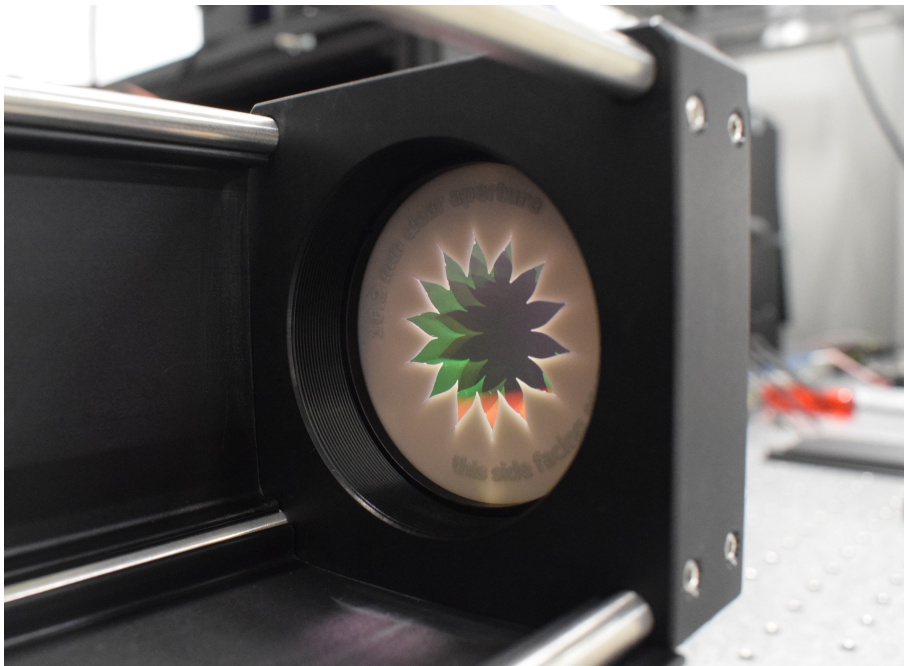# C Photos of the assembled far-field generator
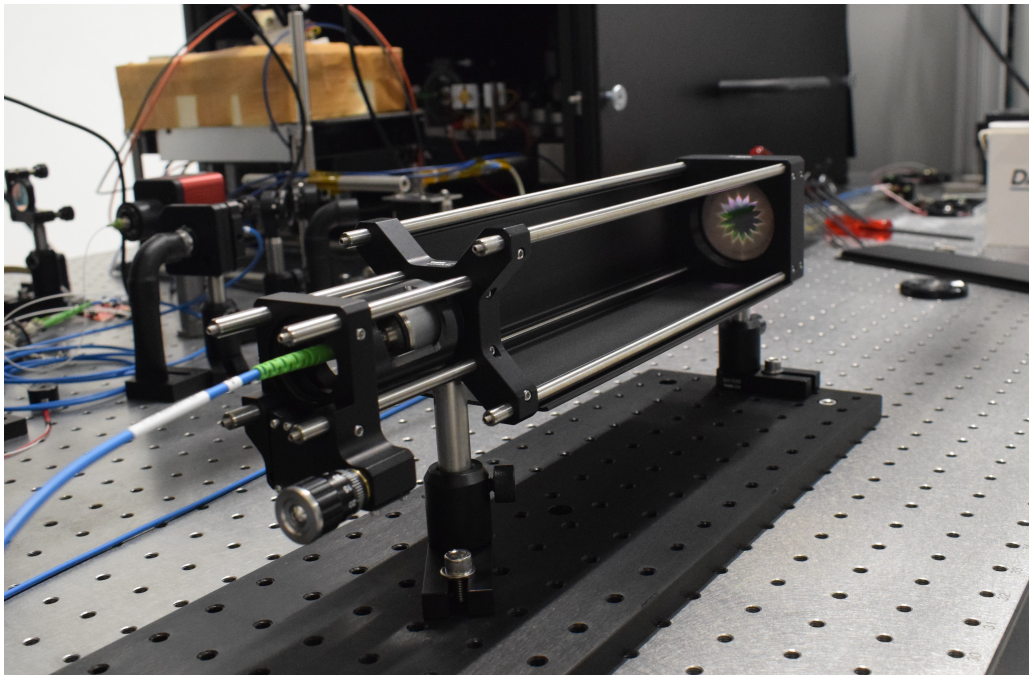
Figure C.1: *Photo of the complete, assembled system with two cage covers removed.*
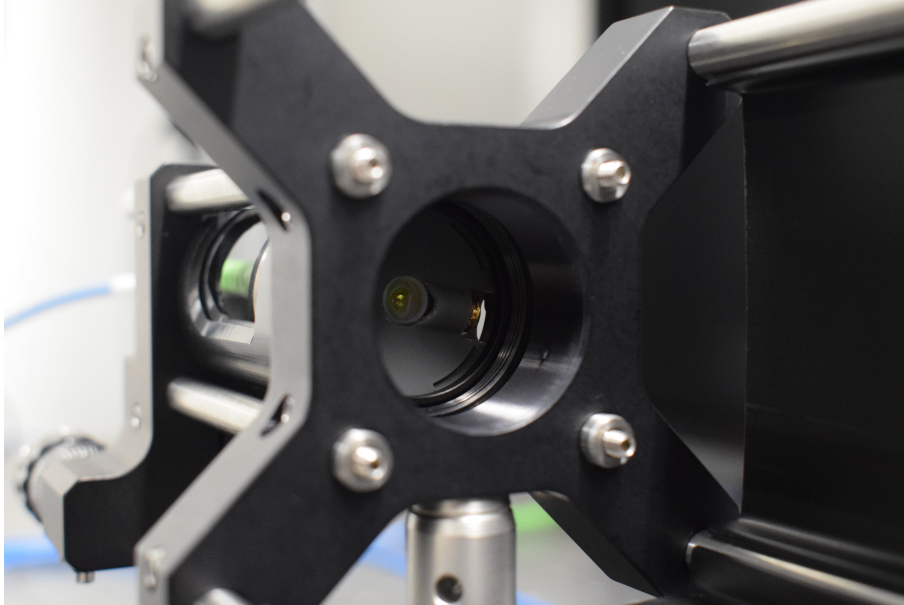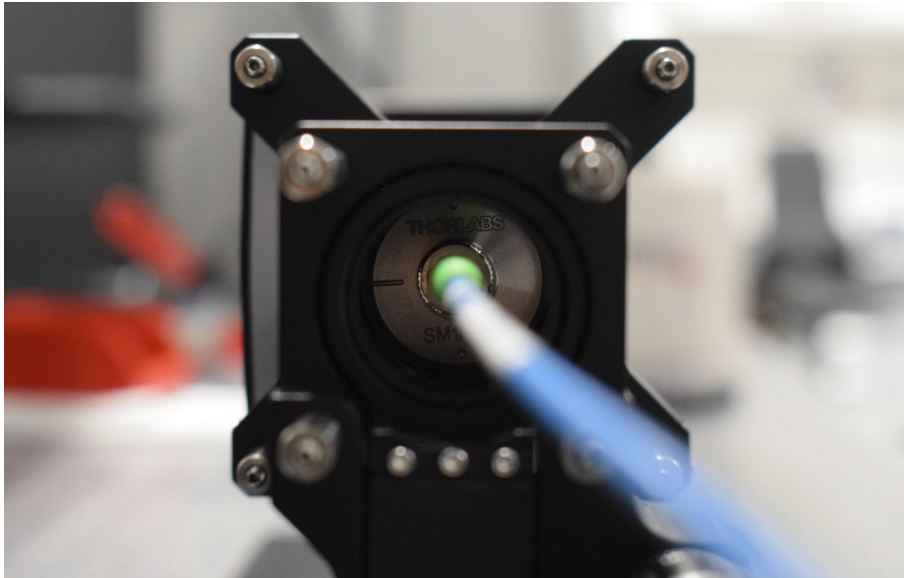
Figure C.2: *Photo of the small-lens adapter inside the lens tube. The lens and the thread insert are visible in the adapter.*
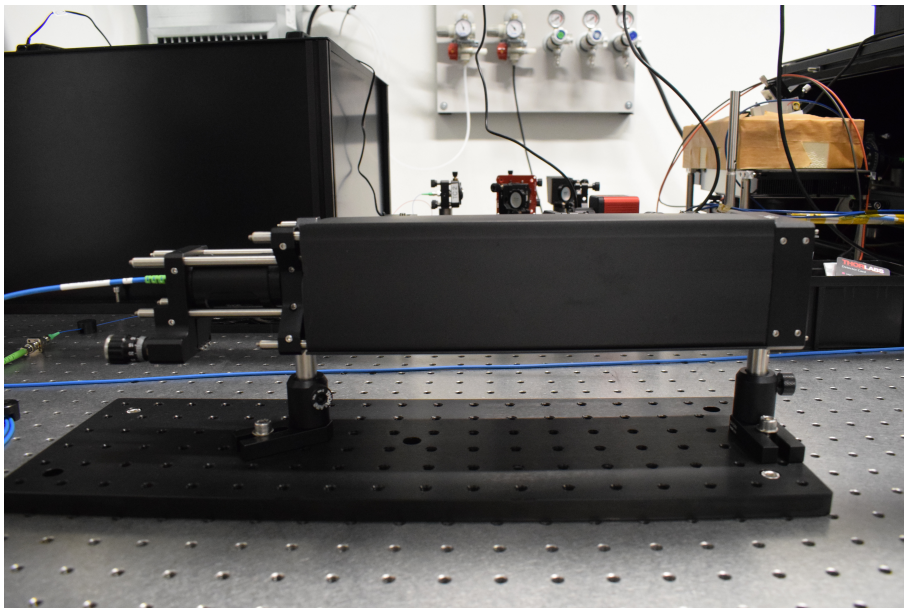

Figure C.3: *Photo of the installed apodizing aperture in front of the collimating lens.*

Figure C.4: *Photo of the terminated fiber adapter inside the lens tube. The marking on the adapter indicates the slow axis of the optical fiber.*

Figure C.5: *Photo of the complete, assembled system with all cage covers installed.*

Contents of the digital appendix

A separate appendix is included in the digital submission of this thesis. It includes measurement results and MATLAB scripts for processing the measured data. It also includes the simulation scripts that yielded the figures in section 2.3.

MATLAB Scripts

This folder contains MATLAB Live Scripts along with the functions and classes of the OSCAR add-on. Included are the scripts for simulating beam propagation through various apertures and the calculation script for analyzing the beam divergence based on the measured intensity data.

Measured Intensity Distribution

This folder contains the results of the intensity measurements in the WinCam File (.wcf) format. It also contains the profiles that were used to create averaged plots and to calculate the beam divergence in textfile (.txt) format.

Measured Wavefronts

This folder contains the results of the wavefront measurements in the collimated beam as HASO RAW image files (.himg) and in textfile (.txt) format.

Conceptual formulation

The topic of the thesis was approved by the examination board of the faculty, based on the following description:

The thesis will cover the development, experimental realization and characterization of an optical far-field generator. The experimental layout will be the basis for the design of a complete optical assembly, which is intended for use as a received beam (RX-beam) in an optical ground support equipment setup. For this purpose, the optical system has to shape a laser beam in such a way, that it imitates the incoming beam from a distant spacecraft in an intersatellite laser interferometer. The initial source will be a laser at a wavelength of 1064 nm contained in an optical fiber with a core diameter of 5.5 µm. The produced beam should evenly illuminate an aperture of 8 mm with a flat intensity profile and a flat wavefront. This way it will mimic an 8 mm section of a laser beam that has propagated much further. To allow for a tilted incidence of the RX-beam, the spot size in the target plane should be no smaller than 10 mm (goal: 15 mm). To facilitate the incorporation into optical test environments, the final optical system should be readily integrated and have a relatively small footprint.